Shear zone evolution and the path of earthquake rupture

Erik M Young[1,2], Christie D. Rowe[1], and James D. Kirkpatrick[1]

[1]Department of Earth & Planetary Sciences, McGill University, 3450 University St., Montréal, QC, H3A 0E8 Canada
[2]Now at: Department of Earth Sciences, Simon Fraser University, 8888 University Dr, Burnaby, BC V5A 1S6

Correspondence: Erik M Young (emyoung@sfu.ca)

Abstract. Plate boundary shear zones generate earthquakes, which are at present unpredictable, but advances in mechanistic understanding of the earthquake cycle offer hope for future advances in earthquake forecasting. Studies of fault zone architecture have the potential to reveal the controls on fault rupture, locking, and reloading that control the temporal and spatial patterns of earthquakes. The Pofadder Shear Zone exposed in the Orange River in South Africa is an ancient, exhumed, paleo-

5 seismogenic continental transform which preserves the architecture of the earthquake source near the base of the seismogenic zone. To investigate the controls on earthquake rupture geometries in the seismogenic crust, we produced a high resolution geologic map of the mylonite zone which forms the shear zone core. The core consists of thin, pinch-and-swell layers of mylonites of variable mineralogic composition, reflecting the diversity of regional rock types which were dragged into the shear zone. Our map displays centimetric bands of a unique black ultramylonite along some mylonite layer interfaces. We present

10 a set of criteria for identifying recrystallized pseudotachylytes (preserved earthquake frictional melts) and show that the black ultramylonite is a recrystallized pseudotachylyte, with its distribution representing a map of ancient earthquake rupture surfaces. We then compare the attributes of lithologic interfaces which hosted earthquakes with those which apparently did not, and find that their geometry differs meaningfully at wavelengths of $\gtrsim 10$ m. We argue that the pinch-and-swell structure of the mylonitic layering, enhanced by viscosity contrasts between layers of different mineralogy, is expected to generate spatially

15 heterogeneous stress during viscous creep in the shear zone, which dictated the path that earthquake ruptures followed. The condition of rheologically layered materials causing heterogeneous stresses should be reasonably expected in any major shear zone, is enhanced by creep, and represents the pre-seismic background conditions through which earthquakes nucleate and propagate. This has implications for patterns of earthquake recurrence and explains why some potential geologic surfaces are favored for earthquake rupture over others.

20 ## 1 Introduction

The small-scale structure of fault zones, especially the local attitude and continuity of pre-existing structures, controls the seismogenic behavior of major fault systems (e.g. Fehler et al., 1987; Thurber et al., 2004; Kaven and Pollard, 2013). The architecture of faults at seismogenic depths is revealed by geological field studies of exhumed structures (Sibson, 1979; Chester et al., 1993; Allen, 2005; Swanson, 2006; Lin et al., 2010; Allen and Shaw, 2011; Rowe et al., 2018). Earthquake relocation

25 techniques enable imaging of earthquake distribution in time and space in active settings (Yang et al., 2011; Savage et al.,

2017). However, it is unusual to be able to examine the overall structure of faults and shear zones including the distribution of seismic slip surfaces (Wibberley et al., 2008).

In continental strike-slip faults, earthquakes nucleate from the shallow brittle crust down to the transition zone below which plastic flow dominates (Sibson, 1982, 1983). The largest earthquakes tend to nucleate near the transition zone, and rupture

30 through the entire seismogenic zone (Sibson, 1980). As a result of ductile deformation, the structure of the fault in the transition zone is distinct from the canonical brittle fault core characterized by one or more discrete principal slip surfaces surrounded by a damage zone (e.g. Chester and Logan, 1986; Caine et al., 1996; Faulkner et al., 2010; Savage and Brodsky, 2011), and is better described as a zone of distributed planar to anastomosing layering, differentiated by distinct mineralogy and fabrics (e.g. Burg and Laurent, 1978; Tobisch et al., 1991; Gerald and Stünitz, 1993; Melosh et al., 2018). Distinct lithologic banding

35 is produced by material heterogeneity on scales from the grain scale (10s-100s μm) to lithologic layering (10s-100s cm), resulting in flow instabilities forming compositional banding (1 – 10s cm, Ishii, 1992; Walcott and Craw, 1993; Goodwin and Tikoff, 2002). These grain-scale to meso-scale fabrics act as guides for seismic waves (Lloyd et al., 2009) and possibly for propagating earthquake ruptures as well (e.g. Swanson, 1988; Allen, 2005; Allen and Shaw, 2013). We use an extraordinary exposure of an ancient seismogenic strike-slip shear zone (Melosh et al., 2014, 2016, 2018) exhumed from the depth of the

40 brittle-plastic transition, to investigate the interaction of shear zone structure with earthquake slip. Using highly detailed outcrop maps (accurate to ∼1 cm) we test for spatial patterns connecting composition and grain size of layering, geometry of layer interfaces, and the occurrence of recrystallized and deformed pseudotachylytes, which are interpreted as paleo-seismic slip surfaces. We find that the pseudotachylytes are not randomly distributed across the shear zone, but are strongly associated with specific wall rock juxtapositions. Pseudotachylyte-bearing contacts have geometric characteristics that distinguish them from

45 pseudotachylyte-absent contacts. We discuss the cause and effect relationships between seismic slip and fault rock evolution in the shear zone on co-seismic to interseismic timescales. We will argue that the interseismic viscous creep processes controlled the architecture of the shear zone and developed the structures that hosted and guided seismic slip, ultimately controlling the strength and patterns of seismicity in this crustal-scale strike-slip shear zone.

2 Geological Setting

50 The Pofadder Shear Zone is a NW - SE striking, transcurrent, dextral shear zone which can be traced nearly 500 km from southern Namibia into northwestern South Africa (Figure 1; Joubert, 1974; Toogood, 1976; Coward, 1980; MacClaren, 1988). The shear zone was active for ∼37-57 Ma (Lambert, 2013) during the last of several regional deformation events that together broadly define the Namaqua Orogeny (Joubert, 1974; Macey et al., 2017). Mineral ages in the Namaqua-Natal Metamorphic Belt indicate that the Namaqua Orogeny comprised at least four distinct deformation events which occurred over a roughly

55 900 Ma period concluding ∼950 Ma ago, characterized by episodic plutonism and metamorphism (Macey et al., 2017). The Pofadder Shear Zone cuts the Richtersveld arc (a terrane within the Namaqua-Natal Metamorphic Belt), which contains Paleoproterozoic orthogneisses and paragneisses, metamorphosed at amphibolite facies and intruded by arc magmas (Macey et al., 2017). The Pofadder Shear zone offset and transposed the peak metamorphic fabrics around 1 Ga (Lambert, 2013).
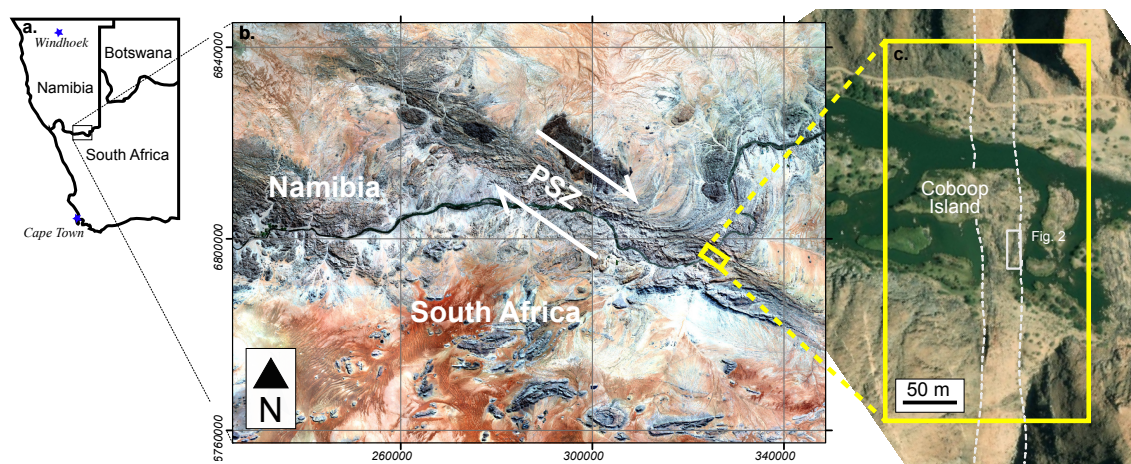
Figure 1. (**a**) Location of study area in region. (**b**) Copernicus Sentinal-2 (2016) imagery of the south-eastern Pofadder Shear Zone (PSZ) striking NW-SE where it crosses the Orange River (Namibia-South Africa border). Yellow rectangle indicates the location of c. (**c**) Coboop Island is only exposed at low water in the Orange River so offers clean bedrock exposure. White dashed lines show approximate edges of shear zone core (Melosh et al., 2018, Fig. 2). White box shows location of high-resolution map of ultramylonite zone on the northeastern edge of the shear zone core (Fig. 2). Background image: (ESRI World Imagery).

In the study area near Pofadder, South Africa (Figure 1), the shear zone is hosted in a series of orthogneissic rocks (the 'Pella
60 Domain' of Macey et al., 2017) including pre-kinematic pink gneisses, gray gneisses, amphibolites, and some hydrothermally altered equivalents (Macey et al., 2017). The study area consists of an exposed shear zone core which is composed of compositionally diverse mylonitic rocks and variably deformed pre- to syn-kinematic pegmatites (Lambert, 2013; Melosh et al., 2018). The exposure surface is on an island within the Orange River only exposed at low water, and is sub-horizontal with minimal topographic relief (<20 cm owing to fluvial erosion), and encompasses the ∼15 m wide layered mylonite-ultramylonite zone
65 on the NE edge of the shear zone core (see Fig. 2 of Melosh et al., 2018).

Mylonite, ultramylonite and pegmatite distinguished by different lithology and grain size form continuous pinch-and-swell layers and locally boudins. The mylonites are commonly isoclinally folded in upright folds with variably plunging axes. A strong subhorizontal rodding lineation is visible on mylonitic foliation surfaces, and the conical rotations of lineations around fold hinges in the mylonites indicate rolling hinges and lineation rotation during differential shearing between different
70 mylonite layers (e.g. Melosh et al., 2018). Evidence of paleoseismicity in the form of pseudotachylytes (Kirkpatrick and Rowe, 2013; Melosh et al., 2014) and dynamic breccias (Melosh et al., 2016) is abundant. Both the pseudotachylyte and dynamic breccias have been shown to be mutually crosscutting with mylonitic foliations, indicating earthquake rupture and plastic creep were broadly coeval during the later stages of shear zone activity at temperatures of 400-500°C, consistent with the deepest seismogenic zone or transition zone (Melosh et al., 2014, 2016, 2018).

3 Composition and structure of the Pofadder Shear Zone core

75

In this section we present methods for small-scale field mapping, and describe the field and microstructural characteristics of the rocks, from which we developed a simplified descriptive scheme for comparing the different mylonites. We then present the arguments supporting recognition of one ultramylonite type as recrystallized pseudotachylyte, and use this identification to gain insight into the seismogenic architecture of the shear zone.

3.1 Methods

80

Mineralogy and fabric of the Pofadder Shear Zone mylonites were documented on multiple scales: $\sim$1 cm – 10 m scales were mapped in the field on drone photography, and μm-mm scales were mapped using optical and electron microscopy.

Field Mapping: For field mapping, we used a DJI Phantom 3 drone flown at 1.5-15 m altitude and hand-held DSLR camera to collect high-resolution images of the outcrop. AGIsoft Photoscan Pro was used to combine the photos into a digital elevation model with draped composite photographs, from which a rectified, georeferenced horizontal orthophoto was extracted. We exported subsets of the orthophoto onto tablets onto which we mapped in the field at a scale of 1:175. We mapped field classified rock types onto the orthophotos (pegmatites, mylonites and ultramylonites). The scale of completion of the maps, for lithologically distinct bodies and contacts, is $\sim$1 cm. Due to low relief (locally, $<$ 20 cm), outcrop surface roughness was neglected as the rectified orthophoto closely approximates a horizontal slice through the geologic structures, containing the average slip vector. Field maps were digitized in ArcGIS from the georeferenced orthophotos. Each contact was classified according to the units it juxtaposed, and the presence or absence of earthquake-indicator features such as pseudotachylyte for subsequent geometric analysis. We sampled each rock type redundantly throughout the field area for microstructural analysis.

Microstructural Component Mapping: A combination of microphotography and image analysis was used to describe lithologic and textural characteristics of different components of the mylonites on a thin section scale in order to compare the grain-scale mineralogy and structure. We used Microsoft Research's Image Composite Editor (ICE) to create composite photomicrographs from optical images and Scanning Electron Microscope (SEM) Backscattered Electron (BSE) images collected using a Phillips XL30 SEM (using 15 keV and spot size 30) to create high resolution grain boundary maps. We divided the thin sections into four major components and determined the relative area of the thin sections comprised of each component using both optical and electron microscopy (Bruker Quantax energy dispersive X-ray microanalysis system (EDS)) in tandem to identify the sub-30 μm matrix phases. Textural and mineralogical data for all samples at all scales were estimated from a 2D sample region and do not necessarily correspond to volume percent of the rock.

3.2 Pofadder Shear Zone mylonites

The shear zone core contains 1-50 cm-thick layers of mylonitic rocks of varying mineralogy, grain size and fabric. For this study we focused on a small area ($\sim$ 960 m^2) in order to map at sufficiently high resolution to resolve the thinnest layers of interest (approximately 1 cm thick). Further subdividing the lithologic classifications of Melosh et al. (2018), we mapped: weakly to moderately foliated pegmatite, quartz mylonite, granitic mylonite and ultramylonite, porphyroclastic mylonite, and black

ultramylonite (Fig. 2, 3). We also present the mineralogical and textural characteristics of a coarser granitic proto-mylonite that is abundant along the shear zone core edges ∼5 m south of the mapping area, to elucidate the progression of mylonitization of the granite wall rock.

110   Pegmatite, granitic mylonite, and quartz mylonite form foliation-parallel pinch-and-swell layers (Fig. 2), locally separating into boudins, on average 20 - 180 cm thick (apparent thickness measured perpendicular to the strike, for subvertical layers). Porphyroclastic mylonite forms pinch-and-swell layers 40 - 90 cm thick and occurs primarily in contact with pegmatite. Black ultramylonite forms < 20 cm thick bands of nearly constant width which are commonly found along interfaces between other lithologies. The interfaces between lithologically and/or texturally distinct layers are sharp, smooth and undulating, sometimes

115 displaying a few centimeters-wide zone of enhanced foliation within the layer on one or both sides of the interface, but without lithologic mixing. We describe the major mineralogy and fabric of each lithology below.

3.2.1 Pegmatite

Undeformed pegmatites are primarily composed of ∼2-5 cm white albitic feldspar crystals which make up approximately ∼90% of the rock, and occasional 1-2 cm quartz crystals and biotite clusters which make up the remaining ∼10% (Figure 3a).

120 Different pegmatite layers display different degrees of foliation intensity, consistent with syn-shearing intrusion along foliation (Lambert, 2013). The foliation is defined by alignment of the long axes of all mineral grains, increase in the aspect ratio of feldspar and quartz grains, and reduced grain size compared to unfoliated pegmatites (Figure 3b). Coarse (1-2 cm) mica grains are observed in weakly foliated pegmatite layers but are absent in moderately- to strongly-foliated pegmatites. The pegmatites are so coarse grained that a small number of crystals can be observed in a thin section, so this rock type was not included in

125 the microstructural analysis.

3.2.2 Quartz mylonite

Quartz mylonite has a metapelitic composition, dominated by alternating bands of quartz and aluminosilicates defining the foliation (Figure 3c) which imparts a cleavage to the rock (Figure 3d). The long axes of crystals and quartz aggregates are parallel with one another and the edges of the bands. The aluminosilicate-rich layers form pinch and swell structures between

130 elongate quartz ribbons. Quartz ribbons are 200 to 500 μm thick, formed from either very fine (∼10 μm) equigranular crystals or elongate ribbon-quartz grains (> 2 mm), exhibiting sweeping undulose extinction. Mica-rich bands have similar thickness to the quartz ribbons, and are composed of extremely fine-grained quartz and pinite (< 5 μm) with occasional remnant coarser muscovite, sillimanite, and cordierite grains (10 - 50 μm) (Figure 4a, b). Slight deformation of pinite pseudomorphs after cordierite is interpreted as evidence for fabric development pre- to syn-retrogression (Figure 4a, b).

135 ### 3.2.3 Granitic mylonite and ultramylonite

Mylonitic rocks of potassic granitic composition (pink orthogneisses), which are the locally predominant wall rock lithology at our study site, contain deformation fabrics that vary from protomylonitic outside the shear zone core, to mylonitic and
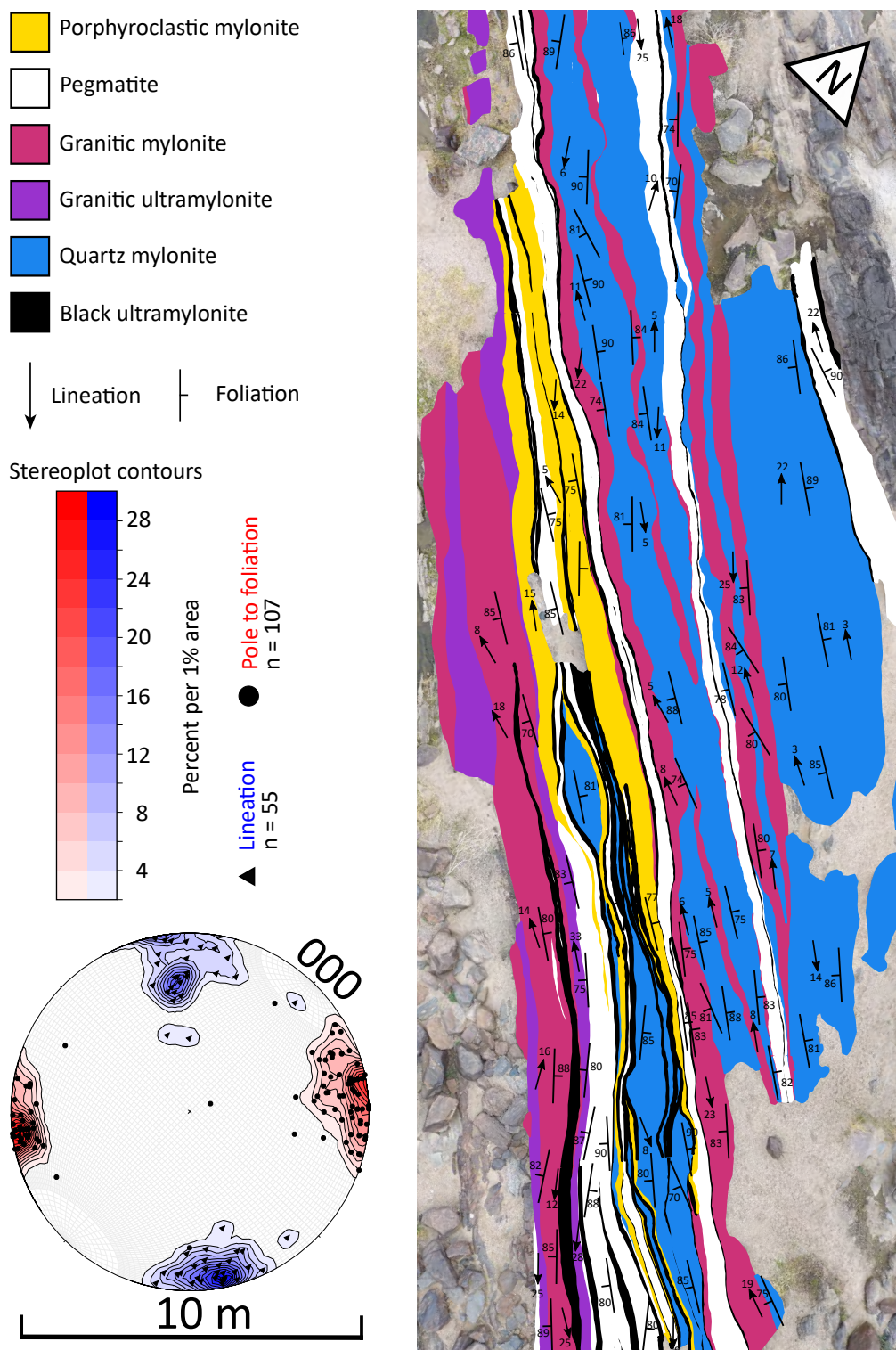
Figure 2. (a) Map of the Coboop Island fault core showing major mylonite units and Quaternary cover highlighted in basemap. Note that symbols are populated based on measurement density, and not all measurements are shown to improve clarity. (b) Stereonet is rotated to match the orientation of the map, and contains contoured measurements of poles to foliation (circles) and lineations (triangles). High resolution basemap and map layers are included as supplementary material.
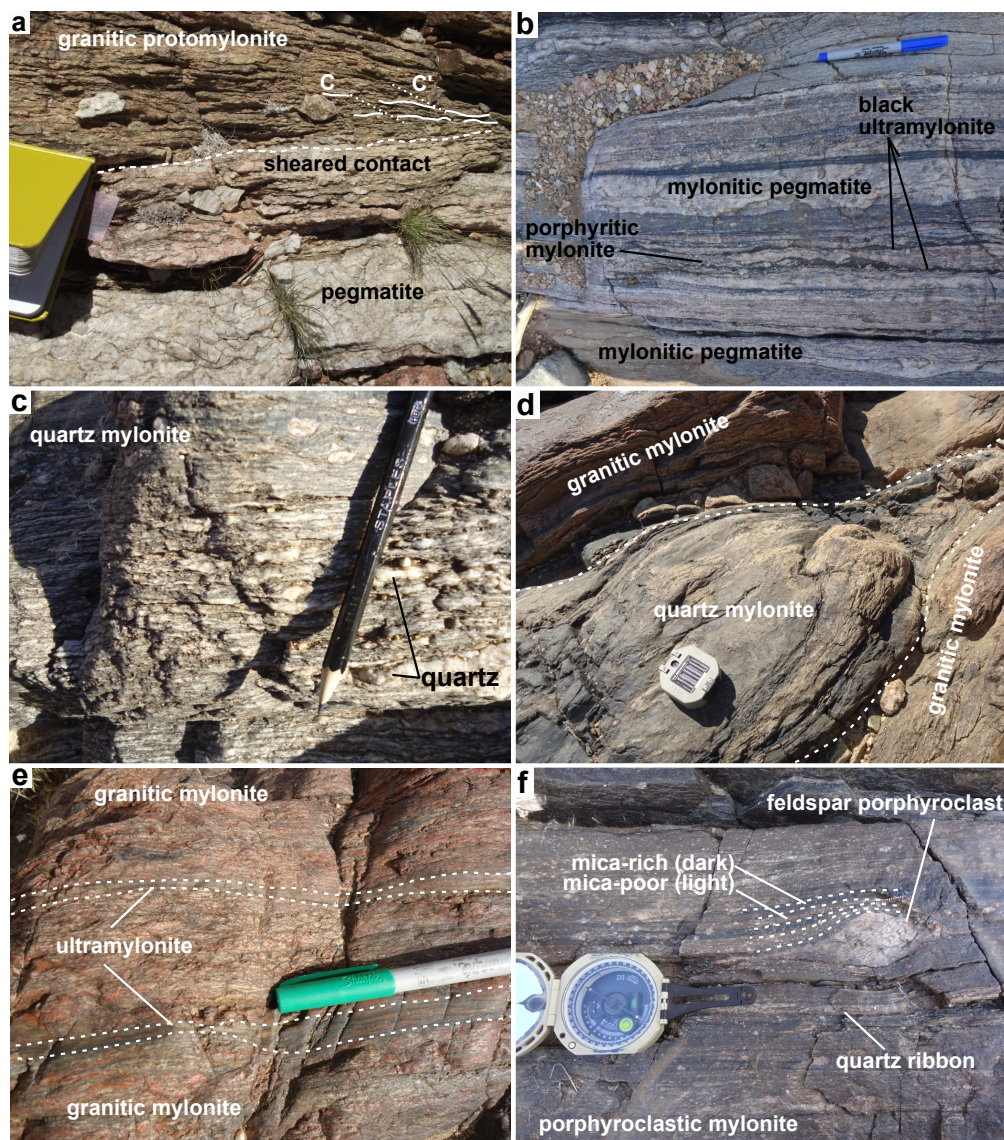
Figure 3. Field photographs of lithologies found in the Coboop Island shear zone core with selected layer interfaces indicated with dotted lines. All photos oriented with dominant foliation (NW) across the photo. (**a**) Granitic protomylonite with sheared intrusive pegmatite contact. Field notebook edge is 12 cm. (**b**) Layers of mylonitic pegmatite, porphyritic mylonite, and black ultramylonite. Pen is 10 mm wide. (**c**) Quartz mylonite with strongly aligned and tailed quartz aggregates, interlayered with aluminosilicate-rich matrix. Pencil is 8 mm wide. (**d**) Boudinaged quartz mylonite contained between layers of granitic mylonite. Compass is 70 mm wide. (**e**) Granitic mylonite cut by granitic ultramylonite horizons. Pen is 10 mm wide. (**f**) Porphyroclastic mylonite with feldspar porphyroclast derived from pegmatite protolith, wrapped by foliation layers of variable mica content. Compass is 70 mm wide.

ultramylonitic within it (Figure 3a, d, e). The mylonitic fabric is defined by millimetric layers of parallel elongated feldspar and quartz. The shear surface foliation (C) is dominant but locally, S-C or C-C' fabrics occur (e.g. Figure 3a). Monomineralic

140   quartz layers 100-1000 μm thick are common, containing equigranular grains with abundant subgrains (subgrain sizes varies

from ~10 μm in the ultramylonite to ~35 μm in the protomylonite). The majority of the porphryoclasts are σ- and δ-clasts of potassium feldspar, or less commonly, quartz (Figure 4e), and dominantly fragmented showing little evidence of crystal plastic deformation. Rare biotite porphyroclasts are ~1-5 mm in size. A strongly lineated and foliated matrix of ~4-6 μm quartz, albite, potassium feldspar and muscovite is present in the mylonite and dominant in the ultramylonite. Ultramylonite displays

145   sub-millimetric tabular straight to gently wavy color banding and is locally transluscent (Figure 3e). Weathered surfaces and fresh surfaces of mylonite are pink to light greyish pink, whereas fresh surfaces of ultramylonite are aphanitic and dark mauve. Proto-mylonites display a rough weathered surface (Figure 7a) and ultramylonites are always very smooth (Figure 3e).

3.2.4   Porphyroclastic mylonite

Porphyroclastic mylonite has an aphanitic matrix with abundant large (up to centimetric) white feldspar porphyoclasts (Figure

150   3b, f). It is usually closely associated with pegmatite layer contacts (Figure 3b). A lineation is defined by elongate feldspar crystals (mainly plagioclase, with less abundant potassium feldspar, <1 - 110 mm) and rare quartz crystals. The matrix is black to greyish-green on weathered surfaces, and light grey to light-pink on fresh surfaces (Figure 3f). Abundant 80 - 500 μm-thick quartz ribbons are occasionally folded, and are composed of ~30μm equigranular grains with abundant subgrains. The majority of porphyroclasts are plagioclase feldspar with minor potassium feldspar, and rarely quartz, forming σ- and

155   δ-clasts which are commonly fragmented. Fragmented feldspar porphyroclasts contain networks of fine-grained mica within the fracture planes indicative of solution assisted breakdown (Figure 4c; Kerrich et al., 1980, 1981). The matrix is composed of ~3-10 μm grains of quartz $\pm$ albite $\pm$ potassium feldspar $\pm$ muscovite (Figure 4c, d). Isolated pores and pore sheets are observed in the matrix (Fig. 4d; c.f. Gilgannon et al., 2021).

3.2.5   Black ultramylonite

160   Black ultramylonite has a black aphanitic matrix containing well-rounded <1 - 20 mm feldspar and quartz porphyroclasts (Figure 3b). The matrix is very mica-rich except for halos around the porphyroclasts, which generally have poorly developed or no tails (Figure 4g, h). Rarely, porphyroclasts are internally fractured. Discontinuous pockets of fine-grained quartz or granitic mylonite are 500 - 1000 μm thick, discontinuous along strike (<15 mm long), and often folded within the matrix. These pockets are composed of either ~ 30 μm equigranular quartz crystals, or occasional prophyroclasts within foliated mylonitic

165   matrix. Compositional banding >100 μm wide is present in the matrix due to varying proportions of biotite $\pm$ muscovite $\pm$ quartz $\pm$ albite, and foliation-parallel strings of very fine-grained ilmenite, with matrix grain sizes of ~5 μm (varying from 1 to 15 μm; Figure 4h). Generally, micas are near-homogeneously distributed within the matrix, and pores are small (few μm) and isolated. Black ultramylonite forms thin layers both within other rock types and along contacts (Figure 3b). This is the only lithology observed cross-cutting foliation planes of other mylonites.
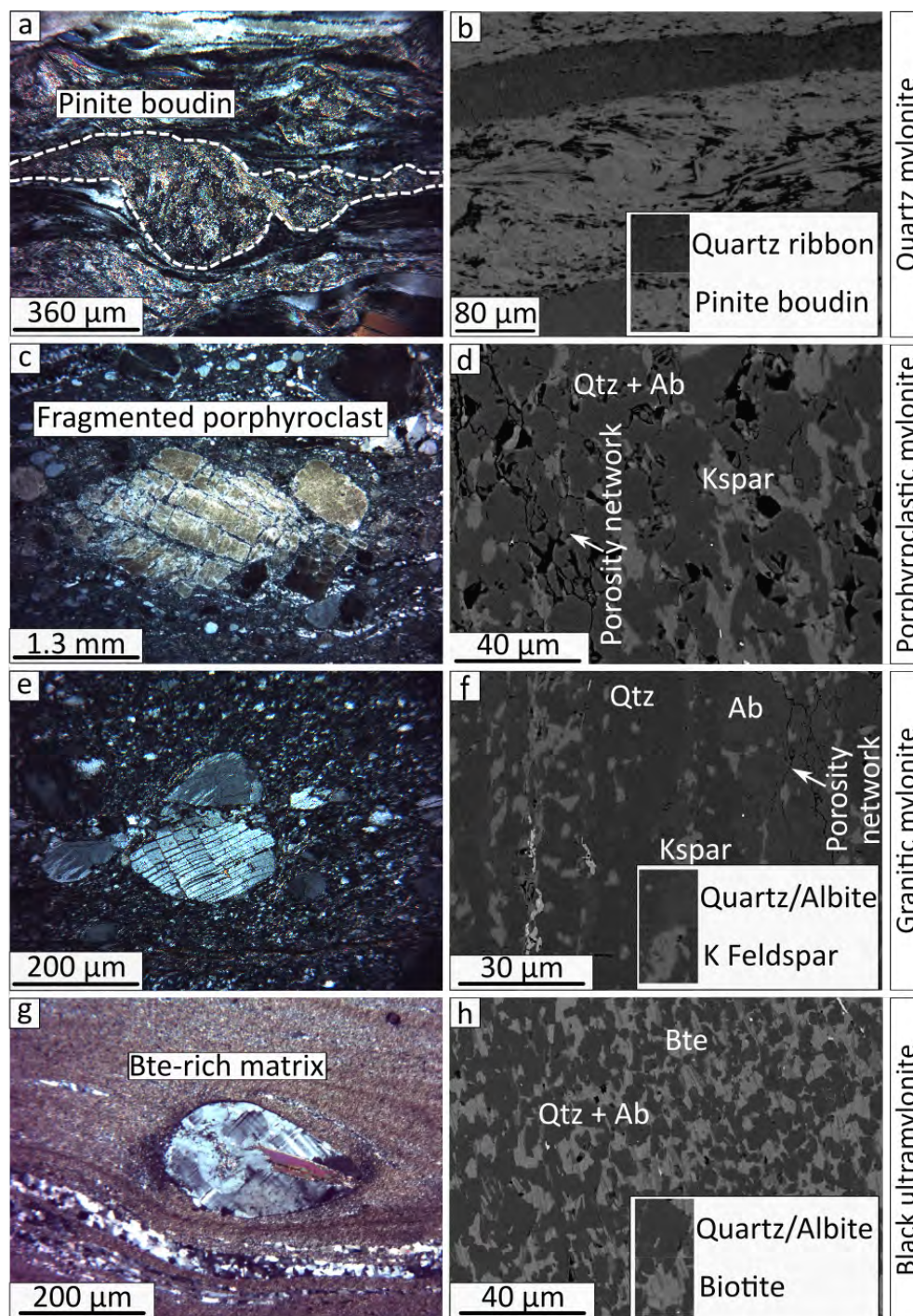
Figure 4. Characteristic microstructure of different Pofadder mylonites (left), with BSE image of fine-grained matrices (right). (**a**) Pinite pseudomorphing boudinaged cordierite in quartz mylonite. (**b**) Pinite band bounded by quartz ribbons. (**c**) Large fragmented porphyroclast of sericite-altered feldspar in porphyroclastic mylonite. (**d**) Quartz/albite (darker grey) and potassium feldspar (medium grey) in the matrix of porphyroclastic mylonite. Intergranular porosity is black. (**e**) Fragmented plagioclase porphyroclast in granitic mylonite. (**f**) Quartz (darkest grey), albite (dark grey) and potassium feldspar (light grey) composing granitic ultramylonite matrix. Intergranular porosity is black and muscovite is white. (**g**) Rounded porphyroclast in black ultramylonite (**h**) Well-distributed biotite (light grey) and quartz/albite (dark grey) matrix in black ultramylonite. Intergranular porosity is black.

9

3.3 Microstructural components of mylonites

In order to relate the field-scale characteristics of the mylonites to mineralogy and microstructure related to deformation behavior, we identified common components occurring in several rock types. We estimated the relative modes of these components using image analysis of photomicrograph mosaics for representative samples. The components are:

1. Quartz ribbons: monomineralic areas of homogeneous recrystallised quartz crystals;

2. Porphyroclasts: coarse grained mono-crystalline clasts surrounded by finer grained material. Includes quartz, feldspars, and rarely micas;

3. Quartz-feldspar-rich matrix: micron-scale polymineralic matrix which constitutes the groundmass surrounding porphyroclasts;

4. Mica-rich matrix: matrix with approximately half mica, half quartz and/or feldspar.
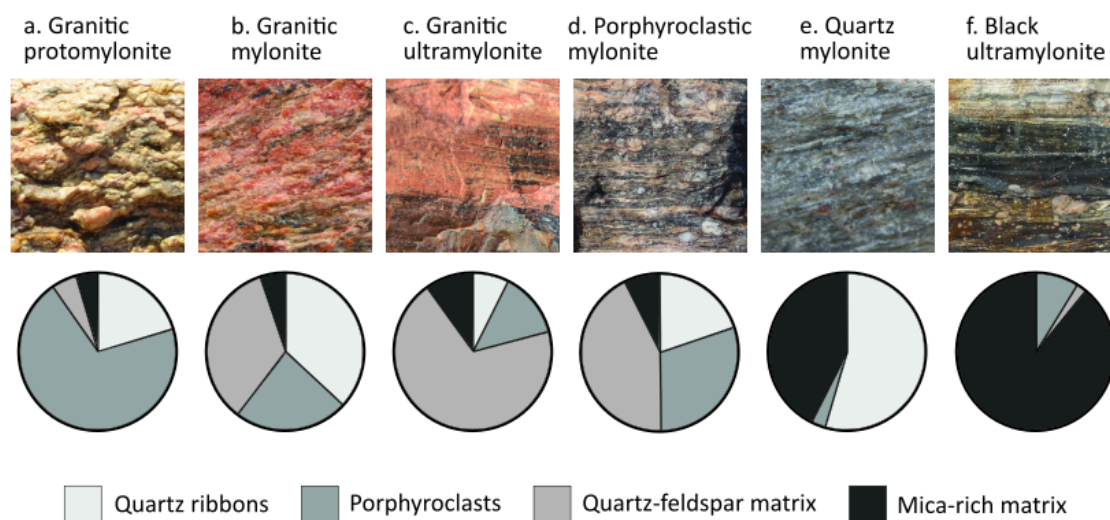

Figure 5. The six rock types which (with pegmatite) dominate the map area, with example photos and pie charts demonstrating the relative proportions of coarse grains (quartz ribbons and porphyroclasts) and fine matrix (divided into quartz-feldspar-rich and mica-rich). Each example photo has a field of view of 3 cm.

Figure 5 reports the relative abundance of the four components in representative thin sections of six rock types. These component modes are consistent with fault rock naming schemes for ductily deformed rocks (e.g. Sibson, 1977). Amongst the granitic mylonites, the trend with decreasing grain size (proto → ultramylonite; Figure 5a-c) is shown by the decrease in porphyroclast content from 70% down to 13% of the rock, and corresponding increase in matrix from 10 up to 80% of the rock. The quartz ribbon content appears to increase between granitic protomylonite to granitic mylonite, but then decrease to 8% in the ultramylonite, possibly due to more efficient phase mixing at the smaller grain size incorporating the quartz into the

background matrix (e.g. Cross and Skemer, 2017). The porphyroclastic mylonite (Figure 5d) is similar to the granitic mylonite, with just under half the rock dominated by very fine matrix, but more abundant quartz ribbons in the granitic matrix and higher proportion of porphyroclasts in the porphyroclastic mylonite. The large porphyroclasts which give the rock its name are notable since they reflect the exceptional bimodality of grain size in the porphyroclastic mylonite, requiring a coarse-grained

190 or porphyroclastic parent rock. The composition, and its common occurrence along the margin of pegmatites (dominated by coarse albite and quartz), suggest that the porphyroclastic mylonite is mostly derived from the pegmatite. The quartz mylonite (Figure 5e) is distinctive, composed of nearly equal parts mica-rich matrix and quartz ribbons. The black ultramylonite (Figure 5f) is overwhelmingly mica-rich with low ($<10\%$) porphyroclast content. The black ultramylonite will be discussed further in Section 3.4.

195 ### 3.4 Identifying recrystallized pseudotachylyte

For this study, it is necessary to identify the surfaces within the Pofadder Shear Zone core which can be shown to have hosted earthquakes. Due to the setting of our study outcrop near the base of the seismogenic zone, the pseudotachylytes formed in this environment are overprinted to some degree by crystal plastic deformation to form ultramylonites (e.g. Passchier, 1982; Clarke and Norman, 1993; Takagi et al., 2000; Price, 2012; Kirkpatrick and Rowe, 2013).

200 #### 3.4.1 Microstructural identification criteria

We have adapted the descriptive criteria developed by previous authors to develop an identification scheme for recrystallized pseudotachylytes in our field area, and use this to distinguish which ultramylonite bands can be shown to represent paleo-earthquake slip surfaces. These criteria are based on the observation that ultramylonites are defined by grain size and matrix proportion (Sibson, 1977), but rocks which develop these attributes may arrive here by two different pathways: one by dy-

205 namic grain size reduction from mylonites during crystal plastic flow, and the other by coarsening and aligned growth from pseudotachylyte (White et al., 1980; Passchier, 1982; Bestmann et al., 2012). The mineralogical and compositional fractionation effects of melting, and distinct contact geometries preserve the difference in the histories of the ultramylonites (Kirkpatrick et al., 2009; Price, 2012; Kirkpatrick and Rowe, 2013).

[ht] Here we present a list of characteristics of ultramylonites which are consistent with, and potentially indicative of,

210 pseudotachylyte origin. The characteristics apply to the matrix, the shape and composition of porphyroclasts, and the layer boundaries. We then compare a variety of distinct ultramylonite samples from our field area to this list.

1. Homogeneous fine grain size in polymineralic matrix (e.g. Passchier, 1982; White, 1996; Ueda et al., 2008; Price et al., 2012) (Figure 6a,c);

2. Preserved flow banding and localized compositional differences within the matrix (e.g. White, 1996; Price et al., 2012);
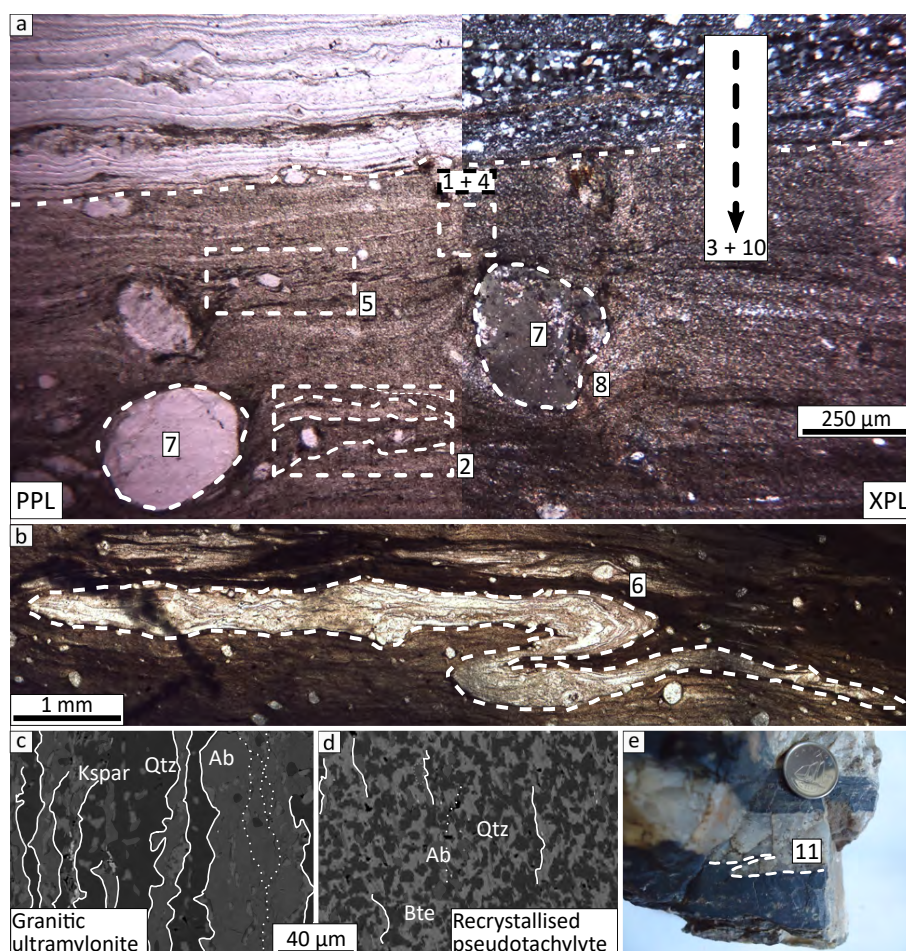
215 3. Ultramylonite layers crosscut wall rock foliation;

Figure 6. Examples of microstructural criteria used to identify recrystallized pseudotachylyte. All images from sample PF01. (**a**) Photomicrograph of ultramylonite (upper half of photo)-pseudotachylyte (lower half of photo) contact, with ppl image on the left and xpl on the right. Numbers refer to criteria in Table 1. (**b**) A fragment of wallrock mylonite is folded and contained within a recrystallised pseudotachylyte matrix. (**c, d**) SEM backscatter images of granitic ultramylonite (**c**) (same as Figure 4f) and black ultramylonite (**d**) (same as Figure 4h) matrices are shown. The interconnected porous horizons (annotated with sparse dashed lines) and phase boundaries extending along multiple grain boundaries (annotated with solid lines) are shown. (**e**) An injection vein is shown in hand sample.

4. Bulk mineralogy of pseudotachylyte usually similar to, or more hydrous (mica-rich) than host rock, and reflects preferential incorporation of hydrous host rock minerals (e.g. Magloughlin, 1989; Pittarello et al., 2012; Kirkpatrick and Rowe, 2013) (Figure 6d);

5. Spatially dispersed opaque minerals (e.g. Magloughlin, 2005; Kirkpatrick and Rowe, 2013)

6. Compositional banding and through-going, interconnected porous grain boundaries are either absent, or rarely extend further than 3-4 grain boundaries (Figure 6c, d; c.f. Mancktelow et al., 1998);

7. Poly-crystalline (often rounded, and occasionally folded) wall rock fragments are commonly contained within the pseudotachylyte matrix preserving truncated pockets of wall rock microstuctures (including foliation and quartz ribbons) (e.g. Figure 6b, Sibson, 1975);

8. Refractory minerals, stronger minerals, and those with weak cleavage are disproportionally represented in porphyroclast population (especially quartz, calcic feldspar relative to alkali; Sibson, 1975; Lin, 1999; Di Toro and Pennacchioni, 2004);

9. Rims of survivor clasts that may coarsen and shear into fine-grained monomineralic mantles and tails during recrystallization, but asymmetric tails are generally poorly developed (Figure 6a; Price et al., 2012) ;

10. Interfaces between pseudotachylyte and host rock may be sharp on a very small ($\sim \mu$m) scale (Figure 6a; Price et al., 2012);

11. Characteristic field geometries of pseudotachylyte (e.g. injection veins) which could form in gouge/cataclasite (Rowe et al., 2012; Kirkpatrick and Rowe, 2013) but which never form in mylonites may be preserved or inferable from deformed geometries (Figure 6e).

3.4.2 Application of criteria for identifying relict pseudotachylyte

Dark-colored ultramylonites with aphanitic matrix in the Pofadder Shear Zone have previously been interpreted as recrystallized and deformed pseudotachylyte (Kirkpatrick and Rowe, 2013; Melosh et al., 2018). By charting the characteristics listed in the previous section, we tested each rock type for match with known characteristics of pseudotachylytes to evaluate the possibility of genetic links. In our study area, there was only one other ultramylonite (pinkish granitic ultramylonite), although there are different colors of granitic ultramylonite elsewhere in the shear zone core (Melosh et al., 2018). We evaluated eight samples of black ultramylonite (Figure 4g) and six samples of granitic ultramylonite (Figure 4e) (Table 1). The black ultramylonite samples matched on average 7.75/10 characteristics for recrystallized pseudotachylyte while the granitic ultramylonites averaged 2.5/10 match. Of the granitic ultramylonites, three samples matched 0-2 characteristics (Table 1). We therefore interpret that the granitic ultramylonites in general do not show characteristics diagnostic of pseudotachylyte origin, and were probably formed by dynamic grain size reduction, whereas the black ultramylonite probably formed through coarsening of pseudotachylytes. Three samples of granitic ultramylonite matched 3 or 4 characteristics, raising the possibility that they could

be recycled pseudotachylytes in advanced stages of recrystallization/deformation so that many of the indicator features have been lost (e.g. Kirkpatrick and Rowe, 2013).

No single criterion divides the two ultramylonites perfectly, although the compositional mica enrichment (criterion 4) and
250 possibly the sharp layer boundaries (criterion 10) may be the strongest discriminators. Polymineralic host rock clasts (criterion 7) were absent from all but one of the granitic ultramylonite samples, and that sample was also the only one to display a preponderance of refractory minerals (e.g. quartz) as clasts, consistent with preservation as survivor grains in a melt. That sample (PF07) also met the most pseudotachylyte criteria (n=4/10) so it is the strongest candidate amongst the granitic ultramylonites to be a 'completely' recycled pseudotachylyte, although it is still a relatively weak match compared to a black ultramylonite
255 sample.

We interpret black ultramylonite strands as recrystallized pseudotachylyte and the product of seismic slip and transient heating, while other ultramylonites are more likely to be derived (or are indistinguishable) from plastic creep of parent mylonites. We therefore confirm the interpretation of Melosh et al. (2014, 2016) that the fault rocks in the PSZ record seismic activity in the brittle-plastic transition zone, and will refer to the black ultramylonites as recrystallized pseudotachylytes, and use the
260 detailed map of black ultramylonites as a map of paleo-earthquake rupture surfaces to examine their distribution.

3.5 Spatial relationships between mylonites and recrystallized pseudotachylyte

The shear zone consists of dozens of parallel bands of mylonites and ultramylonites, creating a very large number of sub-parallel, pre-existing lithologic interfaces which could have been activated during seismic slip. The majority of the lithologic layers pinch and swell and exhibit gently wavy interfaces. This observation is consistent with existing theory on pinch and
265 swell morphologies in deforming viscous layers (Gardner et al., 2015), wherein the shape is controlled by relative competency of the layers, which is a cumulative property influenced by mineralogy, fabric, layer thickness, and grain size of the rocks. However, the recrystallized pseudotachylytes are uniformly a few cm thick, with parallel wavy interfaces and near constant thickness along strike (Figure 2). We classified each interface in our small map area by the lithologies present as wall rocks on either side. The cumulative length of recrystallized pseudotachylyte along contacts between each pair of lithologies was
270 determined as a proportion of the total cumulative length of contacts of the same type. The geometry of the interfaces were then characterized and compared to pseudotachylyte abundance (Table 2, and expressed as length of interface with pseudotachylyte as a percentage of total length of interface between wall rock lithology pairs).

We identify eight interconnected pseudotachylyte networks (black strands in Fig. 2; for definition of pseudotachylyte networks, see Rowe et al., 2018). As the strike-length of the mapped area is only 48 m, likely much smaller than the rupture
275 patches of the paleo-earthquakes that produced the pseudotachylyte, we cannot determine whether the eight identified networks represent different earthquakes or are part of one or more networks which formed in the same earthquake (c.f. Allen, 2005; Rowe et al., 2018). By area, the eight recrystallized pseudotachylyte networks account for ~8% of the mapped fault core. Layers of recrystallized pseudotachylyte are <1 - 13 cm thick (average 5.7 cm). As some of these are significantly thicker than pristine pseudotachylyte fault veins from similar faults (e.g. Sibson, 1975; Sibson and Toy, 2006; Allen and Shaw, 2011; Rowe
280 et al., 2018), these could represent repeated slip of multiple earthquakes along a single slip surface (e.g. Camacho et al., 1995),

Criteria	Description	Black Ultramylonite								Granitic Ultramylonite					
		PS203	PS205	PZ04	PZ18	PZ19	PF01	PF02	PF09	PZ01	PZ02	PZ14	PZ22	PZ24	PF07
Matrix	1. Homogenous fine polymineralic matrix	Y	Y	Y	Y	Y	Y	Y	Y	N	Y	N	Y	Y	Y
Matrix	2. Flow banding & compositional differences	Y	Y	Y	Y	Y	Y	Y	Y	N	N	N	N	Y	Y
Matrix	3. Disruption of host rock layering	Y	Y	Y	Y	Y	Y	Y	N	N	N	N	Y	Y	N
Matrix	4. Mineralogy similar or mica-enriched	Y	Y	Y	Y	Y	Y	Y	N	N	N	N	N	N	N
Matrix	5. Spatially distributed opaques	Y	Y	Y	N	Y	Y	Y	Y	N	Y	Y	Y	Y	N
Matrix	6. Interruption of multi-grain phase and porosity alignment	N/A	N/A	N/A	Y	N/A	Y	N/A	Y	N	N	N	N/A	N/A	N/A
Clasts	7. Host rock clasts	Y	Y	Y	N	N	Y	Y	N/A	N	N	N	N	N	Y
Clasts	8. Types of monomineralic clasts	Y	Y	Y	Y	N	Y	N	Y	N	N	N	N	N	Y
Clasts	9. Limited clast tails	Y	Y	Y	Y	N	Y	Y	Y	N	N	N	N	N	N
Interface	10. Sharp layer boundaries	N/A	N	Y	Y	Y	N/A	Y	N/A	N/A	N/A	N	N/A	N	N
Interface	11. Field geometries e.g. injection veins	N/A	Y	N/A	Y	Y	N	N	N/A	N/A	N/A	N	N/A	N	N
% positive match		100%	90%	100%	82%	70%	90%	80%	75%	0%	22%	9%	38%	40%	40%

Table 1. Results of microstructural comparison of fourteen samples (eight black ultramylonite and six granitic ultramylonite) to the recrystallized pseudotachylyte identification criteria. N/A indicates that it was impossible to assess the criterion in the thin section (e.g. sharpness of layer boundary when the thin section did not contain a layer boundary). Percentage match is calculated with N/A values removed.

or the pseudotachylyte layers were thickened during dynamic recrystallization, by folding and early stages of transposition (e.g. Melosh et al., 2018).

We found that 71% of recrystallized pseudotachylyte is located along an interface between two different lithologies, and 29% occurs within a single lithology. Pseudotachylyte is most abundant along interfaces between porphyroclastic mylonite and pegmatite (72.4%), and between quartz mylonite and porphyroclastic mylonite (71.8%), and less abundant along contacts between pegmatite and either granitic mylonite (61.0%) or quartz mylonite (56.4%) (Table 2). The interface between granitic mylonite and quartz mylonite almost never has pseudotachylyte (2.3%). Finally, while the interface between granitic mylonite and porphyroclastic mylonite also has a low pseudotachylyte occurrence (17.7%), the total length of this type of interface is only 28 meters, making this a lithological relationship with lower occurence than other contact types (56-237 m) within the study area, meaning this percentage may be less representative. The majority of pseudotachylyte with similar wall rock is hosted by pegmatite (41.9% of contact), with decreasing abundance in quartz- (23.4%), granitic- (3.7%), and porphyroclastic (3.1%) mylonite (Table 2).

Wall rocks	Total Length of Contact Type (m)	Pseudotachylyte Length (m)	%	% of all pseudotachy-lytes
Pegmatite & porphyroclastic mylonite	120.0	86.9	72%	21%
Pegmatite & granitic mylonite	149.3	91.0	61%	22%
Pegmatite & quartz mylonite	113.3	63.9	56%	15%
Porphyroclastic mylonite & quartz mylonite	56.2	40.4	72%	10%
Porphyroclastic mylonite & granitic mylonite	28.1	5.0	18%	1%
Granitic mylonite & quartz mylonite	237.1	5.4	2%	1%
Pegmatite (sw)	187.2	78.3	42%	19%
Porphyroclastic mylonite (sw)	133.1	4.0	3%	1%
Granitic mylonite (sw)	156.7	5.8	4%	1%
Quartz mylonite (sw)	146.4	34.4	23%	8%

Table 2. Total length of contacts in mapped area, categorized by the lithologies juxtaposed across the contacts (similar (sw) or different wall rocks), with percentage of total length by wall rock lithology which is decorated by pseudotachylyte. Rows ordered by apparent relative strength.

These data demonstrate that the pseudotachylytes are not randomly distributed across all the possible interfaces in the shear zone core; they are preferentially associated to particular wall rock combinations.

4 Shear zone core mylonite geometry

Some of the rock types in the shear zone core form shorter, higher amplitude boudins, while others tend to flow and fill the space between boudins, producing different interface geometries between different wall rocks. To test the hypothesis that the distribution of pseudotachylyte might be related to the interface geometry, we extracted the interfaces from our field map

for quantitative description and analysis. If interface geometry affects the likelihood of finding pseudotachylyte along an
300 interface, then we should be able to identify a geometric difference between pseudotachylyte-bearing and pseudotachylyte-absent interfaces. We determined the relative competency of the different lithologies based on the shape of the interfaces. We then applied a Fast Fourier transform (FFT) to characterize the shape of contacts for comparison.

4.1 Relative competency from qualitative comparison of layer contact shapes

Differences in the geometry of boudinaged or pinch-swell contacts have been associated with competency contrast in analog
305 models and numerical modelling studies (Cloos, 1947; Ramberg, 1955; Gardner et al., 2015, 2016). The amplitude:wavelength ratio of boudinaged contacts increases with increasing competency contrast, strain, and thickness contrasts, as well as the feedback between viscosity and strain rate which controls stress (Ramberg, 1955; Marques et al., 2012). As all the lithologies in the shear zone are poly-mineralic, directly estimating their strengths from experimentally-derived flow laws is untenable (e.g. Handy, 1994). However, pinch-and-swell curvature reflects the sense of competency contrasts (with the less viscous lithology
310 filling pinches and gaps in the more viscous one; Quirke, 1923; Ramberg, 1955). Combining qualitative observations of layer shape with information on layer thickness can therefore produce a relative hierarchy of lithologic strength during deformation which reflects the local strain rate and stress.

Quartz mylonite layers typically display the largest thickness variations (0 - >1 m), and are commonly observed pinching out completely along strike regardless of the thickness of neighbouring mylonite bands (e.g. Fig. 3d). Granitic mylonite boudins
315 display a lesser thickness variation (up to ∼ 30 cm), and only pinch out completely when layer thickness ratio between this mylonite and surrounding material is >4. Porphyroclastic mylonite and pegmatite layers are not observed pinching out, but do exhibit cyclical changes in thickness on the order of 10-20 cm (Fig. 3a, b). Pinch-swell and boudinage is also observed between layers of the same lithology (especially quartz mylonite) where thickness variation may be the stronger determinant on competency (Figure 2).

320 Based on assessments of composition (encompassing the mineralogy of each mylonite's coarse grained and fine grained microstructural domains, Figure 5), and observations of thickness variations (Figure 2), we define a qualitative hierarchy of competency between the shear zone core lithologies. The geometry of the layer interfaces allows us to rank the different lithologies in terms of relative competence (Gardner et al., 2016). The coarse-grained, plagioclase-dominated pegmatites are more competent than all other rocks in the mylonite zone. The porphyroclastic mylonite (likely derived from dynamic grain
325 size reduction and alteration of the pegmatite) appears to be the second most competent, as it makes cusps along boundaries with the pegmatite (Figure 3A), but the amplitude of its contacts with pegmatite is much lower than the other lithologies against pegmatite (Figure 7). The granitic mylonite appears to be less competent than the porphyroclastic mylonite, based on contact morphology. The quartz mylonite shows higher contact amplitudes than granitic mylonite in contact with the stronger rocks, so was less competent than all the other mylonites. As the quartz mylonite exhibits the thickest layering (Fig. 2), and competency
330 is a function of viscosity and thickness, it is important to control for thickness to establish this as the weakest lithology.

17

4.2 Quantitative mapping and analysis of contact shapes

We selected 14 segments of lithologic interfaces for FFT analysis (Fig. 2). Six of those interface segments are lined with recrystallized pseudotachylyte and eight are sharp contacts between mylonitic wall rocks. The de-trended contacts are presented in Figure 7b-c, where the origin is the northwestern end of each mapped contact. The lengths of layer interfaces (15.1 - 37.2

335 m) vary, and traces are truncated by wall rock changes or pseudotachylyte bifurcations. The amplitude of undulations is $\lesssim 1$ m (across strike distance in Fig. 7b,d). To control for layer thickness, we selected six reference contacts which juxtapose equal-thickness layers (three with pseudotachylyte present, three without; Figure 7c,e).

We calculated the Power Spectral Density (PSD) for each contact trace (Figure 7d, e). This yielded quantitative measures of the power of undulations at different wavelengths along the traces, and allowed us to interpret differences of roughness of

340 these surfaces. Contact traces from the field map were converted into coordinate arrays. The selected interfaces were populated with coordinates at a fixed along-strike interval of 0.05 m through linear interpolation between digitized nodes. The contact geometry was then de-trended to remove the shear zone's northwest-southeast strike from the amplitude component of the digitised contacts. Signal tapering was used to minimize spectral leakage; a forward linear extrapolation (beginning at the trace end point and terminating once extrapolated amplitude matched the trace beginning amplitude) was applied to the de-trended

345 interfaces. Fast Fourier Transforms were performed on converted interfaces in Python 3.7 (utilizing the Numpy library FFT capabilities) to determine the dominant wavelengths of the interface undulations by extracting power spectral density. The input interfaces were zero-padded to increase frequency resolution at low frequencies. Frequencies less than the signal's period length are then discarded.

Our analysis suggests there is a distinct difference between pseudotachylyte-bearing interfaces (cool colors in Figure 7a, d,

350 e) and pseudotachylyte-absent interfaces (warm colors in Figure 7a, b, c). All interfaces exhibit a complex geometry that is represented by multiple sinusoidal components with different wavelengths in the FFT results. In general, the power increases as the wavelength increases. Interfaces decorated by pseudotachylyte (cool colors) display notably larger power compared to interfaces without pseudotachylyte at long wavelengths ($\gtrsim 10$ m). Pseudotachylyte-absent interfaces appear to plateau around an upper power level of ~ 0.4 at wavelengths of 7-10 m. These characteristics of the spectral analysis are qualitatively evident

355 in the detrended interface profiles (Figure 7b,d), where the pseudotachylyte-present interfaces have a geometry dominated by large amplitude, long wavelength components whereas the pseudotachylyte-absent interfaces show lower overall amplitudes and predominance of multiple short wavelength components. This pattern is robust when layer thickness and lithology are controlled, as shown by two pairs of reference contacts with matching wall rock lithologies, (quartz mylonite/pegmatite (red vs. navy blue) and granitic mylonite/pegmatite (orange vs. royal blue); Figure 7).

360 Two of the pseudotachylyte-absent reference interface segments are adjacent segments of one interface mapped across a transition from one wall rock type to another in series (red to orange in Figure 7a). Making the reasonable assumption that the finite strain is similar along the entire interface, the effect of changing one wall rock can be observed (Figure 7d, e). The wall rock on the north side is pegmatite, and on the south, the interface progresses from quartz mylonite in the west (red in Figure 7a) to granitic mylonite in the east (orange in Figure 7a). We observe a reduction in the peak power between the quartz

365   mylonite (red) and granitic mylonite (orange). This amplitude difference is attributable to the difference in competency of the quartz mylonite (weaker) vs. the granitic mylonite (stronger) when they share an interface with pegmatite, the strongest lithology. The interface between quartz mylonite and granitic mylonite (yellow in Figure 7) may have a different finite strain but the high power suggests again that the competency contrast is significant. Comparing each mylonite against the same strong opposing wall rock (pegmatite) is consistent with our qualitative competency hierarchy presented in the previous section.

370   The difference in geometry between pseudotachylyte-bearing and pseudotachylyte-absent contacts remains present when considering all contacts that extend multiple boudin lengths along strike, whether or not we control for layer thickness. The measured power differs for each individual contact, but the predominance of higher power computed for pseudotachylyte-bearing contacts at wavelengths greater than ∼10 meters persists for all 14 contacts.

5   Implications of shear zone mesostructure for the geometry of earthquake rupture

375   Our detailed mapping of the Pofadder Shear Zone core presents the lithologic and architectural complexities of the earthquake source in the deep seismogenic zone. In this section, we reflect on the relationship between interseismic viscous flow and brittle rupture, discuss the possible causes of non-random distribution of pseudotachylytes amongst the layers of mylonites, and speculate on possible effects both on, and due to, earthquake cycles in the middle crust.

5.1   Long-term deformation of mylonitic layering

380   Pinch-and-swell geometries are present in every compositional layer we mapped, which represent the finite deformation within the shear zone, and therefore inform the long-term conditions and processes. As the quartz mylonite, granitic mylonite, and porphyroclastic mylonite are very similar in grain size (Figure 4), but display indications of significant competency contrasts in outcrop, mineralogy seems to be the strongest factor which affected their relative competence during viscous flow. A multitude of grain-scale deformation mechanisms accommodated strain in the mylonites. We commonly observe fragmented feldspar

385   porphyroclasts (dominantly plagioclase) in granitic and porphyroclastic mylonites, which show minimal evidence of dynamic recrystallisation. In all mylonites, the microstructure in monomineralic quartz ribbons (with strong crystallographic preferred orientation; Melosh et al., 2016) suggests that quartz deformed predominantly through dislocation creep. The abundance of flake-shaped pores and co-planar grain boundaries crossing phase boundaries in the mylonite matrices (Figure 4) are consistent with the activity of additional deformation mechanisms, such as grain boundary sliding (e.g. Fliervoet et al., 1997; Fusseis

390   et al., 2009). Syn-kinematic solution-precipitation may also explain the elevated mica contents in the ultramylonites relative to mylonites and to the host rock (e.g. Figure 5; Simpson, 1985; Janecke and Evans, 1988; Fusseis and Handy, 2008; Gilgannon et al., 2017). This complexity of deformation mechanisms makes it impossible to estimate the bulk strengths of individual mylonites from mineralogy and microstructure, but the pinch-and-swell geometries are consistent with power law viscous flow with stress exponents <5 and effective viscosity contrasts on the order of 20-100x (Schmalholz et al., 2008).

395   Our qualitative competency hierarchy (pegmatite > porphyroclastic mylonite > granitic mylonite > quartz mylonite) and the observations of fractured plagioclase porphyroclasts are consistent with plagioclase as the strongest major mineral during
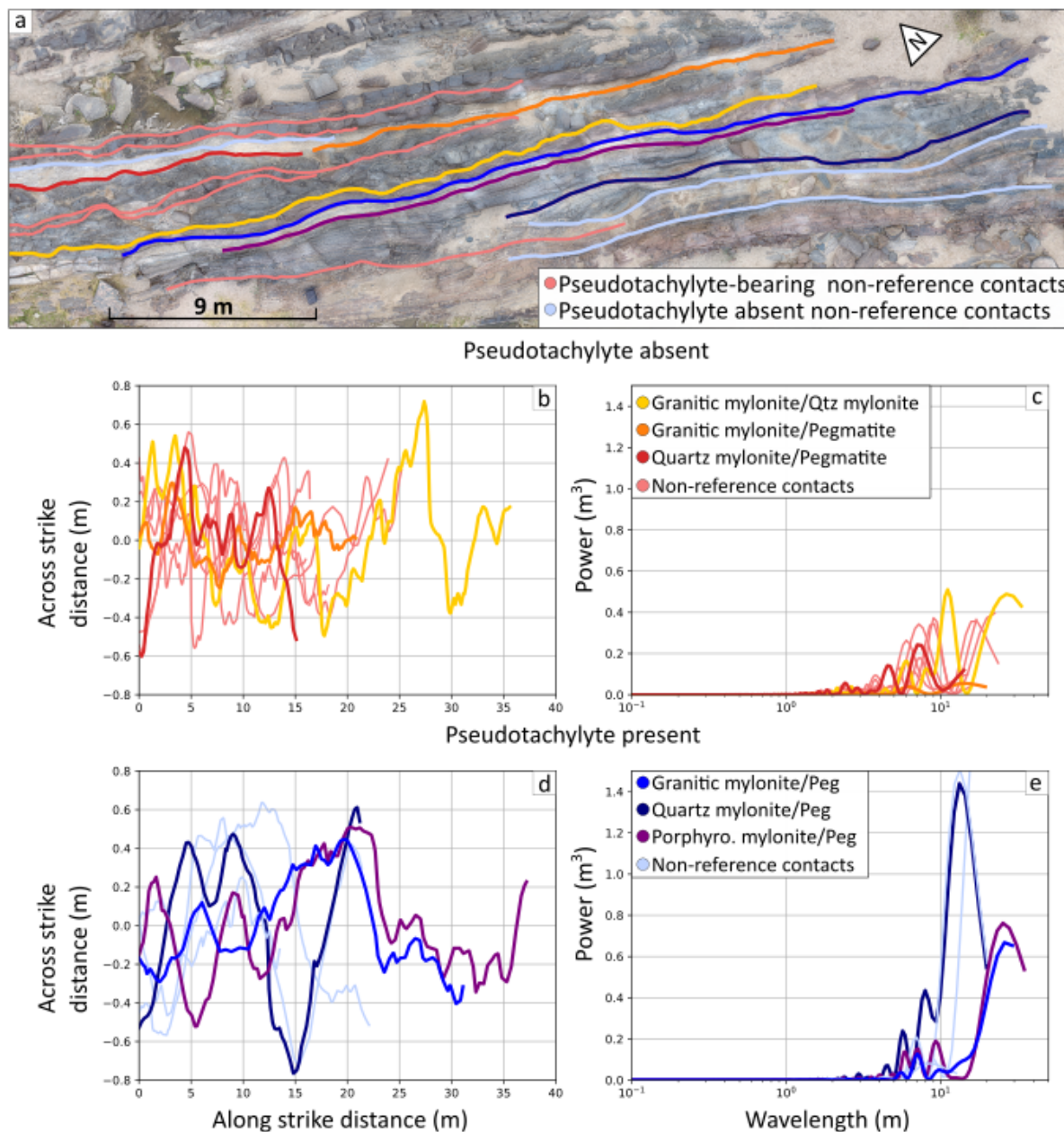
Figure 7. Mylonite layer interface maps. (**a**) Drone image with contact traces deliniated, cool colors have pseudotachylyte and warm colors have no pseudotachylyte. Reference traces of similar wall rock layer thickness are shown in bright colors (see legend for plots) and other interfaces which are not controlled for layer thickness appear in pale colors. Top row of plots shows data for pseudotachylyte-bearing contacts (**b,c**) and bottom row shows pseudotachylyte-absent contacts (**d,e**). (**b,d**): De-trended profiles. (**c,e**) FFT for same contact traces highlights the wavelengths of increased power (m^3).

deformation. The porphyroclastic mylonite retains a higher proportion of plagioclase, while the granitic mylonite contains more quartz and alkali feldspar (Figure 4f vs. d). The weakest mylonite is the quartz mylonite, whose framework is dominated by dynamically recrystallised quartz and mica rather than feldspar. We therefore conclude that the decreasing abundance and

400   grain size of feldspar was the main cause of the inferred decrease in bulk rock viscosity between the lithologies (Figure 5). This has been noted in other granitic shear zones, where replacing feldspar with mica contributed to monotonic weakening in the shear zone core (e.g. Gerald and Stünitz, 1993; Bailey et al., 1994; Wintsch et al., 1995).

Overall, our results demonstrate that in high strain shear zones that contain an array of lithologies and grain sizes, mylonitic layering in the shear zone core is characterized by competency variations that result in wavy interfaces between layers. The

405   Pofadder is typical of mid-crustal shear zones which cut through lithologically heterogeneous crust, with thinned and extended layers of different mineralogies, so we suggest this general structure may be a characteristic of continental transforms in the deep portions of seismogenic zones and transitional zones (e.g. Price et al., 2012; Rennie et al., 2013; Schulte-Pelkum and Mahan, 2014).

5.2   Distribution of preserved earthquakes

410   Pseudotachylytes record myriad paleo-earthquake rupture surfaces passing through the shear zone, predominantly along lithologic interfaces (Table 2). The mylonites are interlayered on a scale of ∼2-60 cm (Figure 2; Melosh et al., 2018), resulting in 10s or 100s of oriented, sub-parallel lithologic interfaces which might have been favourable for earthquake rupture propagation. The observation that pseudotachylytes are mainly located along lithologic interfaces (Table 2), supports the hypothesis that these contacts acted as earthquake guides. Furthermore, if the earthquake ruptures were insensitive to local conditions,

415   such as interface cohesion, rock properties or interface geometry, then we would expect to find the pseudotachylyte distributed randomly amongst the interfaces, but this is not the case. Table 2 shows that some combinations of wall rocks are far more likely to show pseudotachylytes on their interfaces than other combinations.

One possible explanation is that some of the lithologies are more likely to melt during earthquakes, resulting in a pseudotachylyte map which records melting tendency rather than rupture patterns. Mica-rich rocks would be predicted to melt with

420   less frictional heating due to higher water contents and lower melting point (Spray, 2010). This cannot have been the only factor controlling frictional melting in the Pofadder Shear Zone, as some of the highest mica content mylonite (quartz mylonite; Figure 5e) is sometimes associated with the lowest pseudotachylyte abundance interfaces (e.g. granitic mylonite vs. quartz mylonite, which displays only 2.3% pseudotachylyte decoration). The highest melting point of the major rock forming minerals across all mylonites occurs in plagioclase, and the lowest thermal conductivity in quartz (Spray, 2010), resulting in these min-

425   erals overwhelmingly dominating survivor grain populations in pseudotachylytes (Dobson et al., 2018). The higher strength of feldspar-dominated rocks may accentuate frictional heat production (Spray, 1992). Plagioclase is the dominant mineral in pegmatite and porphyroclastic mylonite, a combination which is overwhelmingly favorable for pseudotachylyte (72%). However, high-feldspar contacts between porphyroclastic mylonite and granitic mylonite show low pseudotachylyte abundance. Neither low melting point (mica) nor high frictional heating (plagioclase) can explain the distribution of pseudotachylytes, suggesting

430   that mineralogy has a weak effect. The map of pseudotachylyte is therefore is likely a map of paleo-seismic rupture traces.

The long-term and short-term strength, and the distribution and geometry of lithologic interfaces, are all ultimately controlled mostly by interseismic viscous creep in the shear zone. Below, we assess the influence of different interface characteristics on the distribution of seismic slip in the shear zone.

5.2.1 Interface cohesion

435   It is well known that seismic slip is most likely to occur along pre-existing faults or weak surfaces due to lower cohesion (Hutchinson and Suo, 1991). In the presence of two materials with a cohesionless interface between them, slip is controlled by differences in frictional properties of the materials (Lykotrafitis and Rosakis, 2006), which causes the rotation of local maximum principal stress away from perpendicular to the fault plane. This results in a decrease in the energy required to maintain dynamic slip, and increases displacement for a given stress state (Andrews and Ben-Zion, 1997). Previous field

440 observations of pseudotachlyte-bearing mylonite zones have demonstrated that deformation tends to localize along pre-existing joints, faults or contacts (Di Toro and Pennacchioni, 2005; Shaw and Allen, 2007; Allen and Shaw, 2011; Mittempergher et al., 2021). However, in shear zones, lithologic interfaces are not completely decoupled, as boudin formation, or pinch and swell layer geometries, imply coupling across the interfaces on long time scales (e.g. Abe and Urai, 2012). Our results demonstrate that lithologic interfaces are favored for rupture, but not exclusively, as nearly one third of pseudotachylyte lengths

445 lie between identical wall rocks, so may have ruptured through anisotropic but intact crystalline rock. These observations suggest the interfaces cannot have been completely cohesionless, and the distribution of post-seismic deformation including pseudotachylytes and wall rock indicates that healing after co-seismic melting was effective, with grain growth having occurred during post-seismic healing (c.f. Passchier, 1982; Price et al., 2012; Metteer, 2021). It therefore seems unlikely that cohesion contrasts play a decisive role in controlling the strong preference for earthquake ruptures along some interfaces over others.

5.2.2 Wall rock strength

450

   At the timescale of seismic slip, rupture propagation is not affected by viscous deformation, but is influenced by elastic properties and stress heterogeneities that may pre-exist in the fault zone (Bhat et al., 2010). For example, numerical models suggest that dissimilar elastic properties between wall rocks can lead to variations in normal stress during seismic slip (Dunham and Rice, 2008). As all the mylonites are quartz and feldspar dominated and highly anisotropic, they likely had similar, highly

455 anisotropic elastic moduli (Punturo et al., 2014; Wenning et al., 2018), so differences in elastic properties are unlikely to have determined the distribution of earthquakes. However, the patterns of pinch-and-swell layering imply that a heterogeneous stress distribution existed in the shear zone at any moment during viscous creep (e.g. Abe and Urai, 2012). Previous work on the stress distributions associated with folding and boudinage in power law viscous materials have shown that the magnitude of stress heterogeneities around rigid inclusions can reach 10s-100s MPa (Melosh et al., 2018; Campbell and Menegon, 2019) and

460 perhaps higher during accelerated creep transients (Papa et al., 2020). Furthermore, high contrast interfaces have the largest resolved shear stress during deformation of layered media due to the displacement mismatches across them (Lloyd et al., 1982). In nature, high tractions along a lithologic interface may result in frictional failure (Fagereng et al., 2014; Phillips et al., 2020). We propose that rupture propagation is most favored along pathways with the greatest background shear stress. Pseudo-

tachylytes are most abundant along interfaces with the highest viscosity rocks (e.g. pegmatites) and interfaces with the highest
465   viscosity contrasts (e.g. porphyroclastic mylonite vs. quartz mylonite; Table 2). Thus, the viscosity contrasts contributed to the
development of stress heterogeneity prior to earthquake rupture, which appears to have influenced the locus of seismic slip.

5.2.3   Interface geometry

The maps of interface geometry are 2D, but extend to wavelengths >10 m which are rarely reached in field studies on fault
roughness (e.g. Bistacchi et al., 2011; Candela et al., 2012; Shervais and Kirkpatrick, 2016). Our analyses suggest that the
470   lithologic interfaces are largely indistinguishable at shorter (meters and smaller) wavelengths, with amplitude:wavelength
ratios similar to faults ($\sim 10^{-2} - 10^{-3}$; e.g. Renard et al. (2013); Fang and Dunham (2013)), and with amplitudes that increase
with wavelength in the same way as faults. However, above wavelengths of $\sim$10 m, the pseudotachylyte-bearing interfaces have
amplitudes that exhibit a power law-like scaling with wavelength (steep increase on the log-linear plot), while the interfaces
without pseudotachylyte do not increase appreciably in power with increasing wavelength. The leveling off of the power
475   density above 10 m wavelength may be consistent with progressive boudinage and wavelength-halving as the major control on
the geometry of these pseudotachylyte-absent interfaces (Abe and Urai, 2012). This pattern suggests that earthquake slip was
correlated to interfaces that are rough at long wavelengths.

We considered the possibility that the observed pattern may be the result, rather than the cause, of seismic slip. Where the
layer thickness is constant on either side and the lithologic juxtaposition is the same (e.g. orange vs. royal blue or red vs. navy
480   blue in Figure 7), our data show the pseudotachylye-bearing interfaces have larger amplitudes at long wavelengths. The earth-
quake rupture surfaces are actually rougher than the other, non-seismic lithologic interfaces. Furthermore, the pseudotachylyte-
bearing interfaces that have the same lithology on either side likely ruptured intact rock yet exhibit wavy geometries. This
indicates that the development of the large amplitudes to the pseudotachylyte interfaces may result from a process inherent to
the fracture propagation rather than being completely inherited from the pre-existing interface geometry.

485   It is also possible that the enhanced long-wavelength roughness is caused by the pseudotachylyte itself, if the low strength of
the ultra fine-grained recrystallized pseudotachylyte causes decoupling that interferes with the progression of boudinage along
an interface. Numerical models of boudinage progression between two lithologies with a significant competency contrast have
demonstrated that ongoing shear will lead to the progressive development of shorter wavelength boudins, increasing the range
of wavelengths observed on the interface (Abe and Urai, 2012). If this model accurately represents the process of interface
490   geometric evolution in the Pofadder mylonites, then interfaces with higher finite strain would evolve toward reducing power
at long wavelengths in favor of increasing power at shorter wavelengths. Recrystallized pseudotachylyte is significantly more
micaceous and finer-grained than any of the other mylonites (Figure 5), with distributed mica crystals compared to non-
pseudotachylyte ultramylonites that display mineralogical layering. These attributes predict the lowest bulk viscosity of any of
the lithologies in the shear zone core, and due to the finer grain size, result in the potential for grain boundary sliding dominated
495   strain-accommodation rather than dislocation creep (Fliervoet et al., 1997). Thus, the rheological impact of pseudotachylyte
emplacement may have been to locally weaken the shear resistance and localize ductile deformation into the interface layer

23

of black ultramylonite, effectively decoupling the lithologic interface and impeding the process of wavelength reduction in boudinage.

5.3 Stress heterogeneity, interseismic evolution and earthquakes

500 We suggest that the primary control on the location of earthquake rupture within the Pofadder Shear Zone was pre-rupture stress heterogeneity caused by the geometry variations generated by viscosity contrast between lithologic layers. This is in contrast to frictional faults in the seismogenic zone that may progressively evolve toward smoother, more mature structures (Dascher-Cousineau et al., 2018) which are correlated with greater slip (e.g. Bletery et al., 2016). Earthquakes may behave differently in the conditionally ductile zone, as a result of more complete healing in crystalline rock, and the stress heterogeneity patterns

505 associated with uneven lithologic layering.

Our field observations and interpreted paleo-earthquakes from pseudotachylye occurrence show that structural complexity must have directly impacted the ancient earthquakes, consistent with previous modeling results that suggest the largest earthquakes occur in areas of highest stress heterogeneity (Allam et al., 2019). Aagaard and Heaton (2008) showed that ruptures propagating through heterogeneous stress conditions on a geometrically planar fault would display slip heterogeneity and

510 leave a heterogeneous post-seismic stress field in their wake. Therefore, both interseismic creep and post-seismic stress-drop heterogeneity contribute to keeping stress heterogeneous throughout the seismic cycle.

One mechanism of maintaining co-seismic stress heterogeneity may be the production of a 'drag stress' proportional to the ratio of the slip to the minimum wavelength of roughness (Fang and Dunham, 2013). For reasonable slip magnitudes consistent with moderate continental strike-slip earthquakes (∼0.1 - 1 meter), a rough fault like our pseudotachylyte-bearing

515 faults (amplitude ∼0.1-0.5 m at 10 m wavelengths) should experience drag stress on order 10-100 MPa, approaching 1/3 of the background normal stress at seismogenic depths, and compatible with Fang and Dunham (2013)'s predictions for propagating earthquake ruptures.

Rupture models never approach the small spatial resolution of our field study, so the minimum scale at which stress heterogeneities might affect earthquake rupture is untested numerically (Allam et al., 2019; Bruhat et al., 2020). Milliner et al.

520 (2016) showed that slip variability is correlated with geometric complexity at wavelengths down to ∼200 m. Our observations indicate that we may have captured the lengthscale of transition below which stress heterogeneities are too small to influence earthquake propagation (at scales of <10 m) to the scale at which the effect can be detected (>10 m).

We emphasize that lithologic and geometric heterogeneity are intrinsic to shear zones in the mid crust, which develop progressively and are maintained during deformation. Heterogeneous stress conditions, at scales and magnitudes sufficient to

525 affect rupture distribution, should be expected in the conditionally ductile crust.

6 Summary

This study investigates the distribution of earthquake slip surfaces within a lithologically diverse exhumed continental-scale shear zone using high-resolution geologic mapping of an excellent exposure of the shear zone core from the brittle-ductile

transition zone. We ranked the different types of mylonites in order of their relative competence: the strongest was plagioclase-
rich pegmatite, followed by porphyroclastic mylonite, granitic mylonite, and quartz mylonite was the weakest. We identified
thin layers of black ultramylonite as recrystallised pseudotachylyte networks derived from paleo-earthquake slip and propose
a comprehensive microstructural criteria for differentiating ultramylonites formed by recrystallisation of pseudotachylyte from
ultramylonites formed only through crystal plastic deformation. We have determined that these recrystallised pseudotachylyte
are not randomly distributed, and are concentrated on particular lithologic interfaces associated with the strongest rocks and the
highest strength contrasts between wall rocks. We attribute this pattern to the earthquake-promoting effects of heterogeneous
stress fields associated with geometric complexity generated by viscous boudinage of the heterogeneous mylonite layers. The
paleo-seismic rupture surfaces are distinguished from other lithologic contacts by higher amplitude roughness at length scales
$\gtrsim$10 m, suggesting this is a minimum dimension at which stress heterogeneities may have a significant effect on seismic
rupture processes. Any mid-crustal shear zone of significant strain history is likely to be lithologically banded at depth, this
banding leads to rheologic layering, which leads to pinch-swell geometries, which causes stress concentrations. We suggest
that this environment provides a paradigm for understanding the environment of earthquake nucleation in active continental
faults which could contribute to more naturalistic earthquake cycle models through understanding the interseismic evolution
of the fault zone conditions.

Acknowledgements

Author contributions

CR conceived of the original study and EY/CR co-developed the details. JK lead the acquisition and processing of basemaps,
and EY carried out the field work with contributions from CR and JK. EY performed the field data processing, microscopy, and
microstructural work. EY implemented the quantitative geometric analysis with assistance from JK. The methods were adapted
from code initially developed by JK. EY led the manuscript preparation, with contributions from CR. All authors contributed
to various aspects of the interpretation and edited the manuscript.

560 **Data availability**

The python code and contact traces used for quantitative geometry analysis are available from EY upon request. Samples are stored at the McGill University Department of Earth and Planetary Sciences and available for lending - contact CR.

References

Aagaard, B. T. and Heaton, T.: Constraining fault constitutive behavior with slip and stress heterogeneity, Journal of Geophysical Research: Solid Earth, 113, 2008.

Abe, S. and Urai, J. L.: Discrete element modeling of boudinage: Insights on rock rheology, matrix flow, and evolution of geometry, Journal of Geophysical Research: Solid Earth, 117, 2012.

Allam, A., Kroll, K., Milliner, C., and Richards-Dinger, K.: Effects of fault roughness on coseismic slip and earthquake locations, Journal of Geophysical Research: Solid Earth, 124, 11 336–11 349, 2019.

Allen, J. L.: A multi-kilometer pseudotachylyte system as an exhumed record of earthquake rupture geometry at hypocentral depths (Colorado, USA), Tectonophysics, 402, 37–54, 2005.

Allen, J. L. and Shaw, C. A.: Seismogenic structure of a crystalline thrust fault: Fabric anisotropy and coeval pseudotachylyte–mylonitic pseudotachylyte in the Grizzly Creek shear zone, Colorado, Geological Society, London, Special Publications, 359, 135–151, 2011.

Allen, J. L. and Shaw, C. A.: Seismogenic fault-zone processes and heterogeneity recorded by pseudotachylyte: New insights from the Homestake shear zone, Colorado, in: Classic Concepts and New Directions: Exploring 125 Years of GSA discoveries in the Rocky Mountain Region, edited by Abbott, L. D. and Hancock, G. S., vol. 33 of *Field Guide Series*, pp. 165–183, Geological Society of America, 2013.

Andrews, D. J. and Ben-Zion, Y.: Wrinkle-like slip pulse on a fault between different materials, Journal of Geophysical Research: Solid Earth, 102, 553–571, 1997.

Bailey, C. M., Simpson, C., and De Paor, D. G.: Volume loss and tectonic flattening strain in granitic mylonites from the Blue Ridge province, central Appalachians, Journal of Structural Geology, 16, 1403–1416, 1994.

Bestmann, M., Pennacchioni, G., Nielsen, S., Göken, M., and De Wall, H.: Deformation and ultrafine dynamic recrystallization of quartz in pseudotachylyte-bearing brittle faults: A matter of a few seconds, Journal of Structural Geology, 38, 21–38, 2012.

Bhat, H. S., Biegel, R. L., Rosakis, A. J., and Sammis, C. G.: The effect of asymmetric damage on dynamic shear rupture propagation II: With mismatch in bulk elasticity, Tectonophysics, 493, 263–271, 2010.

Bistacchi, A., Griffith, W. A., Smith, S. A., Di Toro, G., Jones, R., and Nielsen, S.: Fault roughness at seismogenic depths from LIDAR and photogrammetric analysis, Pure and Applied Geophysics, 168, 2345–2363, 2011.

Bletery, Q., Thomas, A. M., Rempel, A. W., Karlstrom, L., Sladen, A., and De Barros, L.: Mega-earthquakes rupture flat megathrusts, Science, 354, 1027–1031, 2016.

Bruhat, L., Klinger, Y., Vallage, A., and Dunham, E. M.: Influence of fault roughness on surface displacement: From numerical simulations to coseismic slip distributions, Geophysical Journal International, 220, 1857–1877, 2020.

Burg, J. and Laurent, P.: Strain analysis of a shear zone in a granodiorite, Tectonophysics, 47, 15–42, 1978.

Caine, J. S., Evans, J. P., and Forster, C. B.: Fault zone architecture and permeability structure, Geology, 24, 1025–1028, 1996.

Camacho, A., Vernon, R., and Gerald, J. F.: Large volumes of anhydrous pseudotachylyte in the Woodroffe Thrust, eastern Musgrave Ranges, Australia, Journal of Structural Geology, 17, 371–383, 1995.

Campbell, L. and Menegon, L.: Transient high strain rate during localized viscous creep in the dry lower continental crust (Lofoten, Norway), Journal of Geophysical Research: Solid Earth, 124, 10 240–10 260, 2019.

Candela, T., Renard, F., Klinger, Y., Mair, K., Schmittbuhl, J., and Brodsky, E. E.: Roughness of fault surfaces over nine decades of length scales, Journal of Geophysical Research: Solid Earth, 117, 2012.

600   Chester, F. and Logan, J. M.: Implications for mechanical properties of brittle faults from observations of the Punchbowl fault zone, Califor-
        nia, Pure and applied geophysics, 124, 79–106, 1986.

        Chester, F. M., Evans, J. P., and Biegel, R. L.: Internal structure and weakening mechanisms of the San Andreas fault, Journal of Geophysical
        Research: Solid Earth, 98, 771–786, 1993.

        Clarke, G. and Norman, A.: Generation of pseudotachylite under granulite facies conditions, and its preservation during cooling, Journal of
605   Metamorphic Geology, 11, 319–335, 1993.

        Cloos, E.: Boudinage, Eos, Transactions American Geophysical Union, 28, 626–632, 1947.

        Copernicus Sentinal-2: Retrieved from ASF DAAC 01/11/2017, processed by ESA, copernicus Sentinal-2 data, 2016.

        Coward, M.: Shear zones in the Precambrian crust of southern Africa, Journal of Structural Geology, 2, 19–27, 1980.

        Cross, A. and Skemer, P.: Ultramylonite generation via phase mixing in high-strain experiments, Journal of Geophysical Research: Solid
610   Earth, 122, 1744–1759, 2017.

        Dascher-Cousineau, K., Kirkpatrick, J. D., and Cooke, M. L.: Smoothing of fault slip surfaces by scale-invariant wear, Journal of Geophysical
        Research: Solid Earth, 123, 7913–7930, 2018.

        Di Toro, G. and Pennacchioni, G.: Superheated friction-induced melts in zoned pseudotachylytes within the Adamello tonalites (Italian
        Southern Alps), Journal of Structural Geology, 26, 1783–1801, 2004.

615   Di Toro, G. and Pennacchioni, G.: Fault plane processes and mesoscopic structure of a strong-type seismogenic fault in tonalites (Adamello
        batholith, Southern Alps), Tectonophysics, 402, 55–80, 2005.

        Dobson, D. P., Thomas, R. W., and Mitchell, T. M.: Diffusion profiles around quartz clasts as indicators of the thermal history of pseudo-
        tachylytes, Geochemistry, Geophysics, Geosystems, 19, 4329–4341, 2018.

        Dunham, E. M. and Rice, J. R.: Earthquake slip between dissimilar poroelastic materials, Journal of Geophysical Research: Solid Earth, 113,
620   http://dx.doi.org/10.1029/2007JB005405, 2008.

        Fagereng, Å., Hillary, G. W., and Diener, J. F.: Brittle-viscous deformation, slow slip, and tremor, Geophysical Research Letters, 41, 4159–
        4167, 2014.

        Fang, Z. and Dunham, E. M.: Additional shear resistance from fault roughness and stress levels on geometrically complex faults, Journal of
        Geophysical Research: Solid Earth, 118, 3642–3654, doi:10.1002/jgrb.50262, 2013.

625   Faulkner, D., Jackson, C., Lunn, R., Schlische, R., Shipton, Z., Wibberley, C., and Withjack, M.: A review of recent developments concerning
        the structure, mechanics and fluid flow properties of fault zones, Journal of Structural Geology, 32, 1557–1575, 2010.

        Fehler, M., House, L., and Kaieda, H.: Determining planes along which earthquakes occur: method and application to earthquakes accompa-
        nying hydraulic fracturing, Journal of Geophysical Research: Solid Earth, 92, 9407–9414, 1987.

        Fliervoet, T. F., White, S. H., and Drury, M. R.: Evidence for dominant grain-boundary sliding deformation in greenschist-and amphibolite-
630   grade polymineralic ultramylonites from the Redbank Deformed Zone, Central Australia, Journal of Structural Geology, 19, 1495–1520,
        1997.

        Fusseis, F. and Handy, M.: Micromechanisms of shear zone propagation at the brittle–viscous transition, Journal of Structural Geology, 30,
        1242–1253, 2008.

        Fusseis, F., Regenauer-Lieb, K., Liu, J., Hough, R., and De Carlo, F.: Creep cavitation can establish a dynamic granular fluid pump in ductile
635   shear zones, Nature, 459, 974–977, 2009.

        Gardner, R., Piazolo, S., and Daczko, N.: Pinch and swell structures: evidence for strain localisation by brittle-viscous behaviour in the
        middle crust, Solid Earth, 6, 1045, 2015.

Gardner, R. L., Piazolo, S., and Daczko, N. R.: Shape of pinch and swell structures as a viscosity indicator: Application to lower crustal polyphase rocks, Journal of Structural Geology, 88, 32–45, 2016.

640 Gerald, J. F. and Stünitz, H.: Deformation of granitoids at low metamorphic grade. I: Reactions and grain size reduction, Tectonophysics, 221, 269–297, 1993.

Gilgannon, J., Fusseis, F., Menegon, L., Regenauer-Lieb, K., , and Buckman, J.: Hierarchical creep cavity formation in an ultramylonite and implications for phase mixing, Solid Earth, 8, 1193–1209, 2017.

Gilgannon, J., Waldvogel, M., Poulet, T., Fusseis, F., Berger, A., Barnhoorn, A., and Herwegh, M.: Experimental evidence that viscous shear
645 zones generate periodic pore sheets, Solid Earth, 12, 405–420, 2021.

Goodwin, L. B. and Tikoff, B.: Competency contrast, kinematics, and the development of foliations and lineations in the crust, Journal of Structural Geology, 24, 1065–1085, 2002.

Handy, M. R.: Flow laws for rocks containing two non-linear viscous phases: a phenomenological approach, Journal of Structural Geology, 16, 287–301, 1994.

650 Hutchinson, J. W. and Suo, Z.: Mixed mode cracking in layered materials, Advances in applied mechanics, 29, 63–191, 1991.

Ishii, K.: Partitioning of non-coaxiality in deforming layered rock masses, Tectonophysics, 210, 33–43, 1992.

Janecke, S. U. and Evans, J. P.: Feldspar-influenced rock rheologies, Geology, 16, 1064–1067, 1988.

Joubert, P.: The gneisses of Namaqualand and their deformation, South African Journal of Geology, 77, 339–345, 1974.

Kaven, J. O. and Pollard, D. D.: Geometry of crustal faults: Identification from seismicity and implications for slip and stress transfer models,
655 Journal of Geophysical Research: Solid Earth, 118, 5058–5070, 2013.

Kerrich, R., Allison, I., Barnett, R. L., Moss, S., and Starkey, J.: Microstructural and chemical transformations accompanying deformation of granite in a shear zone at Mieville, Switzerland; with implications for stress corrosion cracking and superplastic flow, Contributions to Mineralogy and Petrology, 73, 221–242, 1980.

Kerrich, R., La Tour, T., and Barnett, R.: Mineral reactions participating in intragranular fracture propagation: implications for stress corrosion
660 cracking, Journal of Structural Geology, 3, 77–87, 1981.

Kirkpatrick, J., Shipton, Z., and Persano, C.: Pseudotachylytes: rarely generated, rarely preserved, or rarely reported?, Bulletin of the Seismological Society of America, 99, 382–388, 2009.

Kirkpatrick, J. D. and Rowe, C. D.: Disappearing ink: How pseudotachylytes are lost from the rock record, Journal of Structural Geology, 52, 183–198, 2013.

665 Lambert, C. W.: Granitic melt transport and emplacement along transcurrent shear zones: Case study of the Pofadder Shear Zone in South Africa and Namibia, Msc thesis, Stellenbosch University, 2013.

Lin, A.: Roundness of clasts in pseudotachylytes and cataclastic rocks as an indicator of frictional melting, Journal of Structural Geology, 21, 473–478, 1999.

Lin, A., Ren, Z., and Kumahara, Y.: Structural analysis of the coseismic shear zone of the 2008 M_w7.9 Wenchuan earthquake, China, Journal
670 of Structural Geology, 32, 781–791, 2010.

Lloyd, G., Ferguson, C., and Reading, K.: A stress-transfer model for the development of extension fracture boudinage, Journal of Structural Geology, 4, 355–372, 1982.

Lloyd, G. E., Butler, R. W., Casey, M., and Mainprice, D.: Mica, deformation fabrics and the seismic properties of the continental crust, Earth and Planetary Science Letters, 288, 320–328, 2009.

675 Lykotrafitis, G. and Rosakis, A.: Dynamic sliding of frictionally held bimaterial interfaces subjected to impact shear loading, in: Proceedings of the Royal Society of London A: Mathematical, Physical and Engineering Sciences, vol. 462, pp. 2997–3026, The Royal Society, 2006.

MacClaren, A.: The geology of the area east of Pofadder with emphasis on shearing associated with the Pofadder Lineament, Northwest Cape, Master's thesis, University of Cape Town, 1988.

Macey, P. H., Thomas, R. J., Minnaar, H. M., Gresse, P. G., Lambert, C. W., Groenewald, C. A., Miller, J. A., Indongo, J., Angombe, M., 680 Shifotoka, G., Frei, D., Diener, J. F. A., Kisters, A. F. M., Dhansay, T., Smith, H., Doggart, S., Le Roux, P., Hartnady, M. I., and Tinguely, C.: Origin and evolution of the ∼1.9 Ga Richtersveld Magmatic Arc, SW Africa, Precambrian Research, 292, 417–451, 2017.

Magloughlin, J. F.: The nature and significance of pseudotachylite from the Nason terrane, North Cascade Mountains, Washington, Journal of Structural Geology, 11, 907–917, 1989.

Magloughlin, J. F.: Immiscible sulfide droplets in pseudotachylyte: Evidence for high temperature (> 1200 C) melts, Tectonophysics, 402, 685 81–91, 2005.

Mancktelow, N. S., Grujic, D., and Johnson, E. L.: An SEM study of porosity and grain boundary microstructure in quartz mylonites, Simplon Fault Zone, Central Alps, Contributions in Mineralogy and Petrology, 131, 78–85, 1998.

Marques, F. O., Fonseca, P. D., Lechmann, S., Burg, J.-P., Marques, A. S., Andrade, A. J. M., and Alves, C.: Boudinage in nature and experiment, Tectonophysics, 526-529, 88–96, 2012.

690 Melosh, B. L., Rowe, C. D., Smit, L., Groenewald, C., Lambert, C. W., and Macey, P.: Snap, Crackle, Pop: Dilational fault breccias record seismic slip below the brittle–plastic transition, Earth and Planetary Science Letters, 403, 432–445, 2014.

Melosh, B. L., Rowe, C. D., Gerbi, C., Bate, C. E., and Shulman, D.: The spin zone: Transient mid-crust permeability caused by coseismic brecciation, Journal of Structural Geology, 87, 47–63, 2016.

Melosh, B. L., Rowe, C. D., Gerbi, C., Smit, L., and Macey, P.: Seismic cycle feedbacks in a mid-crustal shear zone, Journal of Structural 695 Geology, 112, 95–111, 2018.

Metteer, S.: Strength implications of recycled pseudotachylyte fault veins within mylonites of the Norumbega Shear Zone, Southern Maine, USA, Masters thesis, McGill University, 2021.

Milliner, C., Sammis, C., Allam, A., Dolan, J., Hollingsworth, J., Leprince, S., and Ayoub, F.: Resolving fine-scale heterogeneity of co-seismic slip and the relation to fault structure, Scientific reports, 6, 1–9, 2016.

700 Mittempergher, S., Zanchi, A., Zanchetta, S., Fumagalli, M., Gukov, K., and Bistacchi, A.: Fault reactivation and propagation in the northern Adamello pluton: The structure and kinematics of a kilometre-scale seismogenic source, Tectonophysics, p. 228790, 2021.

Papa, S., Pennacchioni, G., Menegon, L., and Thielmann, M.: High-stress creep preceding coseismic rupturing in amphibolite-facies ultra-mylonites, Earth and Planetary Science Letters, 541, 116 260, 2020.

Passchier, C.: Pseudotachylyte and the development of ultramylonite bands in the Saint-Barthelemy Massif, French Pyrenees, Journal of 705 Structural Geology, 4, 69–79, 1982.

Phillips, N. J., Motohashi, G., Ujiie, K., and Rowe, C. D.: Evidence of localized failure along altered basaltic blocks in tectonic mélange at the updip limit of the seismogenic zone: Implications for the shallow slow earthquake source, Geochemistry, Geophysics, Geosystems, 21, e2019GC008 839, 2020.

Pittarello, L., Pennacchioni, G., and Di Toro, G.: Amphibolite-facies pseudotachylytes in Premosello metagabbro and felsic mylonites (Ivrea 710 Zone, Italy), Tectonophysics, 580, 43–57, 2012.

Price, N. A.: Structure and rheology of the Sandhill Corner shear zone, Norumbega fault system, Maine: A study of a fault from the base of the seismogenic zone, Phd thesis, University of Maine, 2012.

Price, N. A., Johnson, S. E., Gerbi, C. C., and West Jr, D. P.: Identifying deformed pseudotachylyte and its influence on the strength and evolution of a crustal shear zone at the base of the seismogenic zone, Tectonophysics, 518, 63–83, 2012.

715 Punturo, R., Cirrincione, R., Fazio, E., Fiannacca, P., Kern, H., Mengel, K., Ortolano, G., and Pezzino, A.: Microstructural, compositional and petrophysical properties of mylonitic granodiorites from an extensional shear zone (Rhodope Core complex, Greece), Geological Magazine, 151, 1051–1071, 2014.

Quirke, T. T.: Boudinage, an unusual structural phenomenon, Bulletin of the Geological Society of America, 34, 649–660, 1923.

Ramberg, H.: Natural and experimental boudinage and pinch-and-swell structures, The Journal of Geology, 63, 512–526, 1955.

720 Renard, F., Candela, T., and Bouchaud, E.: Constant dimensionality of fault roughness from the scale of micro-fractures to the scale of continents, Geophysical Research Letters, 40, 83–87, 2013.

Rennie, S., Fagereng, Å., and Diener, J.: Strain distribution within a km-scale, mid-crustal shear zone: the Kuckaus Mylonite Zone, Namibia, Journal of Structural Geology, 56, 57–69, 2013.

Rowe, C. D., Kirkpatrick, J. D., and Brodsky, E. E.: Fault rock injections record paleo-earthquakes, Earth and Planetary Science Letters, 335,
725 154–166, 2012.

Rowe, C. D., Ross, C., Swanson, M. T., Pollock, S., Backeberg, N. R., Barshi, N. A., Bate, C. E., Carruthers, S., Coulson, S., Dascher-Cousineau, K., Harrichhausen, N., Peña Castro, A. F., Nisbet, H., Rakoczy, P., Scibek, J., Smith, H., Tarling, M. S., Timofeev, A., and Young, E.: Geometric complexity of earthquake rupture surfaces preserved in pseudotachylyte networks, Journal of Geophysical Research: Solid Earth, 123, 7998–8015, 2018.

730 Savage, H. M. and Brodsky, E. E.: Collateral damage: Evolution with displacement of fracture distribution and secondary fault strands in fault damage zones, Journal of Geophysical Research: Solid Earth, 116, 2011.

Savage, H. M., Keranen, K. M., Schaff, D., and Dieck, C.: Possible precursory signals in damage zone foreshocks, Geophysical Research Letters, 2017.

Schmalholz, S. M., Schmid, D. W., and Fletcher, R. C.: Evolution of pinch-and-swell structures in a power-law layer, Journal of Structural
735 Geology, 30, 649–663, 2008.

Schulte-Pelkum, V. and Mahan, K. H.: Imaging faults and shear zones using receiver functions, Pure and Applied Geophysics, 171, 2967–2991, 2014.

Shaw, C. A. and Allen, J. L.: Field rheology and structural evolution of the Homestake shear zone, Colorado, Rocky Mountain Geology, 42, 31–56, 2007.

740 Shervais, K. A. and Kirkpatrick, J. D.: Smoothing and re-roughening processes: The geometric evolution of a single fault zone, Journal of Structural Geology, 91, 130–143, 2016.

Sibson, R.: Fault rocks and fault mechanisms, Journal of the Geological Society, 133, 191–213, 1977.

Sibson, R.: Transient discontinuities in ductile shear zones, Journal of Structural Geology, 2, 165–171, 1980.

Sibson, R. H.: Generation of pseudotachylyte by ancient seismic faulting, Geophysical Journal International, 43, 775–794, 1975.

745 Sibson, R. H.: Fault rocks and structure as indicators of shallow earthquake source processes, in: Proc. Conf. VIII on Analysis of Actual Fault Zone in Bedrock, Open-File Rept. 79, vol. 1239, pp. 276–304, 1979.

Sibson, R. H.: Fault zone models, heat flow, and the depth distribution of earthquakes in the continental crust of the United States, Bulletin of the Seismological Society of America, 72, 151–163, 1982.

Sibson, R. H.: Continental fault structure and the shallow earthquake source, Journal of the Geological Society, 140, 741–767, 1983.

750 Sibson, R. H. and Toy, V. G.: The habitat of fault-generated pseudotachylyte: Presence vs. absence of friction-melt, in: GEOPHYSICAL
      MONOGRAPH-AMERICAN GEOPHYSICAL UNION, edited by Abercrombie, R., McGarr, A., Di Toro, G., and Kanamori, H., vol.
      170, p. 153, AGU AMERICAN GEOPHYSICAL UNION, 2006.

Simpson, C.: Deformation of granitic rocks across the brittle-ductile transition, Journal of structural geology, 7, 503–511, 1985.

Spray, J. G.: A physical basis for the frictional melting of some rock-forming minerals, Tectonophysics, 204, 205–221, 1992.

755 Spray, J. G.: Frictional melting processes in planetary materials: From hypervelocity impact to earthquakes, Annual Review of Earth and
      Planetary Sciences, 38, 221–254, 2010.

Swanson, M. T.: Pseudotachlyte-bearing strike-slip duplex structures in the Fort Foster Brittle Zone, S. Maine, Journal of Structural Geology,
      10, 813–828, 1988.

Swanson, M. T.: Late Paleozoic strike-slip faults and related vein arrays of Cape Elizabeth, Maine, Journal of Structural Geology, 28, 456–
760   473, 2006.

Takagi, H., Goto, K., and Shigematsu, N.: Ultramylonite bands derived from cataclasite and pseudotachylyte in granites, northeast Japan,
      Journal of Structural Geology, 22, 1325–1339, 2000.

Thurber, C., Roecker, S., Zhang, H., Baher, S., and Ellsworth, W.: Fine-scale structure of the San Andreas fault zone and location of the
      SAFOD target earthquakes, Geophysical Research Letters, 31, 2004.

765 Tobisch, O. T., Barton, M. D., Vernon, R. H., and Paterson, S. R.: Fluid-enhanced deformation: transformation of granitoids to banded
      mylonites, western Sierra Nevada, California, and southeastern Australia, Journal of Structural Geology, 13, 1137–1156, 1991.

Toogood, D. J.: Structural and metamorphic evolution of a gneiss terrain in the Namaqua Belt near Onseepkans, South West Africa, Ph.D.
      thesis, University of Cape Town, 1976.

Ueda, T., Obata, M., Di Toro, G., Kanagawa, K., and Ozawa, K.: Mantle earthquakes frozen in mylonitized ultramafic pseudotachylytes of
770   spinel-lherzolite facies, Geology, 36, 607–610, 2008.

Walcott, C. R. and Craw, D.: Subsolidus physical and chemical mixing of granite and gabbro during mylonitization, South Victoria Land,
      Antarctica, Journal of structural geology, 15, 1433–1441, 1993.

Wenning, Q. C., Madonna, C., de Haller, A., and Burg, J.-P.: Permeability and seismic velocity anisotropy across a ductile–brittle fault zone
      in crystalline rock, Solid Earth, 9, 683–698, 2018.

775 White, J. C.: Transient discontinuities revisited: pseudotachylyte, plastic instability and the influence of low pore fluid pressure on deforma-
      tion processes in the mid-crust, Journal of Structural Geology, 18, 14711 479–14771 486, 1996.

White, S., Burrows, S., Carreras, J., Shaw, N., and Humphreys, F.: On mylonites in ductile shear zones, Journal of Structural Geology, 2,
      175–187, 1980.

Wibberley, C. A., Yielding, G., and Di Toro, G.: Recent advances in the understanding of fault zone internal structure: a review, Geological
780   Society, London, Special Publications, 299, 5–33, 2008.

Wintsch, R., Christoffersen, R., and Kronenberg, A.: Fluid-rock reaction weakening of fault zones, Journal of Geophysical Research: Solid
      Earth, 100, 13 021–13 032, 1995.

Yang, H., Zhu, L., and Cochran, E. S.: Seismic structures of the Calico fault zone inferred from local earthquake travel time modelling,
      Geophysical Journal International, 186, 760–770, 2011.